





# Assessing thermohydraulic performance in novel micro pin-fin heat sinks: A synergistic experimental, agile manufacturing, and machine learning approach

Mohammad Harris <sup>\*</sup> , Hamza Babar, Hongwei Wu <sup>\*</sup> 

School of Physics, Engineering and Computer Science, University of Hertfordshire, College Lane Campus, Hatfield, AL10 9AB, UK

## ARTICLE INFO

### Keywords:

Heat transfer  
Micro pin-fins  
Mini and microchannels  
Machine learning  
Thermal management

## ABSTRACT

As advancements in technology and rapid product development redefine engineering paradigms, this study examines the influence of innovative and bio-inspired designs on heat transfer efficiency. The research evaluates the thermohydraulic performance of new biomorphic pin fins employing various strategic approaches and agile manufacturing techniques to optimise the design process. Experimental assessments were conducted on four hybrid pin fin configurations within Reynolds Numbers ranging from 101 to 507 and power outputs of 150 W and 250W. The investigation focused on how different geometrical features impact critical performance metrics, including the Nusselt Number, thermal resistance, and pressure drop. Results indicate a significant enhancement in heat transfer performance, ranging from 25 % to 45 %, compared to traditional designs, even at lower Reynolds Numbers and energy consumption levels. Additionally, new empirical correlations were developed specifically for these hybrid designs. Machine learning models demonstrated high accuracy in predicting the Nusselt Number, using Reynolds and Prandtl Numbers as key variables, achieving a mean absolute percentage error (MAPE) of less than 3.5 % and an  $R^2$  value exceeding 0.95. Among the models evaluated, XGBoost, Random Forest, and Polynomial Regression exhibited superior performance with both real and synthetic data. This study underscores the potential of unconventional biomorphic geometries, highlighting the benefits of agile manufacturing and cutting-edge technologies in optimising resource use and improving predictive accuracy. The findings advocate for a reassessment of traditional heat sink designs and propose promising directions for future research in advanced sustainable thermal management.

## 1. Introduction

Currently, thermal management is beyond just a technical necessity and is a critical factor for success and sustainability. For instance, in electronic devices, cooling is fundamental to preventing overheating and safeguarding the reliability and lifespan of smartphones, microprocessors, and high-performance computing systems [1]. Similarly, the aerospace sector relies heavily on precise thermal control to ensure optimal performance and aircraft safety. Also, the automotive industry sees significant benefits from advanced thermal management, which enhances engine efficiency and extends the battery life of electric vehicles [2]. Effective heat transfer and management can boost machinery efficiency and reduce energy consumption in industrial settings.

Various cooling technologies and thermal management strategies have been introduced to address these sustainable needs. These range

from traditional methods like heat sinks [3], film and flow boiling [4,5], and nanomaterials [6] to more sophisticated approaches such as microchannel heat exchangers, heat pumps, and synthetic jet cooling combined with the current state-of-the-art in machine learning and artificial intelligence [7]. Among these, micro pin-fins (MPF) stand out due to their capacity to expand the surface area and generate turbulence, making them a crucial technology in thermal management [8]. However, as electronic devices continue to shrink and power densities climb, relying solely on traditional pin-fin geometries is unsuitable [9].

Recent works have highlighted a significant amount of research on pin-fin-based heat sinks, with a reliance on traditional geometries [1,10,11]. However, the prevalence of MPFs and non-conventional or combined and hybrid pin-fins is an area that requires much more attention to gain a comprehensive understanding of their effectiveness for optimal performance [8]. Peles et al. [12] were among the first to examine micro-pin fins; they investigated heat transfer and pressure drop

<sup>\*</sup> Corresponding authors.

E-mail addresses: [m.harris8@herts.ac.uk](mailto:m.harris8@herts.ac.uk) (M. Harris), [h.wu6@herts.ac.uk](mailto:h.wu6@herts.ac.uk) (H. Wu).

<https://doi.org/10.1016/j.ijheatmasstransfer.2024.126581>

Received 2 September 2024; Received in revised form 4 December 2024; Accepted 12 December 2024

Available online 16 December 2024

0017-9310/© 2024 The Authors. Published by Elsevier Ltd. This is an open access article under the CC BY license (<http://creativecommons.org/licenses/by/4.0/>).

Nomenclature			
<i>Latin Symbols</i>			
A	Area, m <sup>2</sup>	b	base
C <sub>p</sub>	Specific heat capacity, J/kg·K	f	fluid
D	Diameter, m	F	fin
D <sub>h</sub>	Hydraulic diameter, m	in	inlet
h	Heat transfer coefficient, W/m <sup>2</sup> K	o	outlet
H	Height, m	s	surface
K	Thermal conductivity, W/m·K	th	thermal
L	Length, m	ts	test section
m <sup>·</sup>	Mass flow rate, kg/s		
N	Number of points		
Nu	Nusselt number, no unit	<i>Abbreviations</i>	
Q	Heat energy rate, W/m <sup>2</sup>	CFD	Computational Fluid Dynamics
Pr	Prandtl Number, no unit	CFAS	Cruciform Flower with Astroid Splitters
Pu	Pumping power use, W	CFSM	Cruciform Flower with Secondary Mini/Microchannels
R <sub>th</sub>	Thermal resistance, K/W	CM	Combined Model
Re	Reynolds number, no unit	DV	Dependent Variable
SA	Surface area, m <sup>2</sup>	EFE	Exocoetidae -inspired with Filleted Edges
T	Temperature, C/K	EN	Elastic Net
u	Directional velocity, m/s	ESE	Exocoetidae -inspired with Sharp Edges
V	Volume, m <sup>3</sup>	HTC	Heat Transfer Coefficient
W	Width, m	IV	Independent Variable
Z	Random variable	KNN	K-nearest Neighbours
		LR	Linear Regression
		MAPE	Mean Absolute Percentage Error
		MLP	Multilayer Perceptron
		MPF	Micro Pin-Fin
		MPFHS	Micro Pin-Fin Heat Sinks
		MLR	Multiple Linear Regression
		MSE	Mean Squared Error
		PIF	Performance Improvement Factor
		PLR	Polynomial Regression
		RF	Random Forest
		RR	Ridge Regression
		SVR	Support Vector Regression
		XGB	XGBoosting
<i>Greek Symbols</i>			
η	Efficiency, dimensionless		
μ	Fluid viscosity, kg/m·s		
ρ	Fluid density, kg/m <sup>3</sup>		
δ	Rate of change		
σ	Standard deviation		
<i>Subscripts/Superscripts</i>			
a	air		

phenomena in a micro pin-fin bank. A simplified expression for total thermal resistance has been derived, discussed, and experimentally validated. The study examined the impact of geometrical and thermo-hydraulic parameters on total thermal resistance, finding that pin-fin heat sinks can achieve very low thermal resistances comparable to those in microchannel convective flows. An increase in flow temperature significantly reduced thermal resistance. Also, another initial research by Siu-ho et al. [13] tested a copper micro pin-fin heat sink (MPFHS), finding that existing low Reynolds number correlations were inaccurate, highlighting the need for further research into MPF thermal and fluid dynamics — this is arguably still the case in recent years.

Shemelash et al. [14] addressed microprocessor cooling challenges by designing Fibonacci phyllotaxis circular MPFHSs. They used multi-objective optimisation and factorial experiments to determine optimal parameters: 300 μm height, 122.6 μm diameter, and 130 μm phyllotaxis coefficient, with a coolant velocity of 2.263 m/s. This design achieved a maximum temperature of 51.6 °C and a pumping power of 0.191 W, showcasing superior heat dissipation. Xu et al. [15] followed a similar bio-inspired MPF strategy. They investigated petaloid and placoid MPFs, inspired by Clematis Montana and Squalus Acanthias; they analysed thermal-hydraulic characteristics under different conditions and found petaloid fins provided better heat transfer but higher flow resistance, while placoid fins had lower resistance but less heat transfer. Moreover, a new correlation for the Nusselt number and friction factor showed deviations below 2.0 % and 4.5 %, respectively.

Roosbehi et al. [16] optimised the MPF geometry for improved performance. They varied the vertex angle and relative length and found

that a vertex angle of 60° and a relative length of 1 provided the best results. This design improved fluid flow, reducing recirculation and thermal boundary layer effects, and increased the average Nusselt number by 24.46 % and thermal performance factor by 23.89 % at a Reynolds number of 1000. Qidwai et al. [17] combined microjets and MPF in a cooling system, optimising geometric parameters such as jet diameter to pin fin diameter ratio, jet diameter to standoff distance, and pin fin pitch. They found that vortex generation significantly influenced heat transfer, achieving optimal performance at specific geometric ratios. The jet Reynolds number had minimal impact on performance.

Gupta et al. [18] used numerical simulations and NSGA-II to optimise perforated MPFs with square shapes and circular perforations. They focused on maximising the Nusselt number and minimising the friction factor while varying design variables. The study found perforations did not affect stiffness and provided insights into thermohydraulic features, enhancing the understanding of complex cooling systems. Harris et al. [19] also numerically compared square MPFs with a novel biomorphic scutoid pin-fin design under different wall-heating conditions. The results showed that the scutoid design outperforms traditional pin-fins, achieving a higher heat transfer coefficient with lower pressure drop and operating base temperatures. Wall heating improved heat distribution but reduced overall heat dissipation; pressure drop was more influenced by pin-fin geometry than wall heating conditions. Also, Xie et al. [20] studied staggered diamond MPFs in microchannels, analysing pressure drop and heat transfer characteristics. They found stable vortex-wake flow at low Reynolds numbers, but instability at higher Reynolds numbers affected heat transfer,

highlighting the importance of vorticity and turbulent kinetic energy in heat transfer.

Micro pin-fins have also been used in combination with refrigerants. Xu et al. [21] developed a petaloid micro pin-fin heat sink (MPFHS) to improve microelectronic cooling. They compared the performance of green refrigerants R1234ze(E) and R1234yf with R134a. R1234ze(E) showed the highest heat transfer coefficient and lowest frictional pressure drop. New correlations were created for the petaloid design, achieving mean deviations of 12.6 % for heat transfer and 9.9 % for pressure drop. Likewise, David et al. [22] investigated a micro pin-fin microchannel heat sink using R134a refrigerant. They found the heat sink maintained nearly uniform temperatures and showed a peak heat transfer coefficient at an exit vapour quality of 0.55. Their study introduced a cost-effective technique for enhanced cooling performance.

Additionally, some researchers have investigated micro-pin fins with nanofluids. For instance, Ambreen et al. [23] investigated how pin-fin shapes and nanofluids affect heat transfer in heat sinks. Nanofluids improved performance for all pin-fin shapes, with circular fins performing best. At maximum pressure drop, nanofluids led to significant enhancements in heat transfer, with circular, square, and triangular fins achieving Nusselt number improvements of 23.1 %, 16.5 %, and 8 %, respectively. On a separate occasion, Ambreen et al. [24] used a two-phase Eulerian-Lagrangian model to evaluate a MPFHS with water and nanofluids. They found nanofluids improved thermal performance, with the highest average heat transfer coefficient enhancement of 16 % at higher particle concentrations and optimal pressure drop. Also, Keshavarz et al. [25] explored the effects of nanofluids and fin distribution on heat sink performance. Drop-shaped fins increased outlet temperature slightly but reduced pumping work compared to circular fins. Nanofluids like  $\text{Al}_2\text{O}_3$ -water improved performance, and staggered fin arrangements provided higher temperatures but required more pumping work than in-line configurations.

MPFs are also utilised in flow boiling studies. Markal et al. [26] investigated the effect of inlet temperature on the boiling performance of two heat sinks: a conventional micro-pin-fin (HS-1) and an expanding pin-fin design (HS-2). HS-2 outperformed HS-1 due to its micro-pin-fin structure, which prevents bubble blockage and promotes efficient heat transfer. The expanding flow passages in HS-2 also enhance micro convection by accelerating bubble movement, further improving thermal and hydraulic performance. In another investigation, Markal and Evcimen [27] compared the transient performance of a micro-pin-fin heat sink (MD) with a conventional parallel wall heat sink (SD). MD outperforms SD with faster thermal stabilisation, higher heat transfer coefficients, lower surface temperatures, and reduced pressure drops. MD's design prevents dry-out and bubble confinement, enhances nucleation, and improves flow stability. Despite higher pressure fluctuations, MD consistently delivers superior thermal and hydraulic performance, especially at lower inlet temperatures.

Microfluidics cooling is another area where MPF are utilised. Rajan et al. [28] demonstrated microfluidic cooling for 2.5-D system-in-packages using integrated MPFHSs and 3-D printed manifolds. This approach effectively cooled an FPGA, maintaining core temperatures around 30 °C while dissipating 107 W of power, with a thermal resistance of 0.074 °C/W, showing promise for high-power applications. Sarvey et al. [29] examined microfluidic cooling with a MPFHS integrated into an FPGA. Using deionized water, they achieved an average junction-to-inlet thermal resistance of 0.07 °C/W, effectively cooling the FPGA and demonstrating the feasibility of this method for high-density electronic applications. Zhang et al. [30] designed a TSV-compatible MPFHS for high-power 3-D IC stacks, maintaining chip temperatures below 50 °C at power densities over 100 W/cm<sup>2</sup>. Their design achieved a 33 % reduction in junction temperature compared to air cooling, demonstrating effective cooling for advanced ICs. Renfer et al. [31] utilised vortex-enhanced heat transfer in 3D chip stacks using TSVs and MPFs. They achieved up to 230 % increase in local Nusselt numbers and reduced temperature non-uniformity significantly,

improving overall thermal performance by up to 190 %.

Other investigations to assess the MPFHS performance were by Shi et al. [32] who explored different nozzle shapes for a composite heat sink to manage high heat fluxes in chip technology. They found that diamond nozzles achieved the highest local heat transfer coefficient but had poor performance on the MPF surface. Square nozzles offered the best overall performance with lower thermal resistance and pressure drop, demonstrating effective cooling for high-heat flux chips. Han et al. [33] studied subcooled flow boiling in MPF arrays under varying conditions. They observed that the heat transfer coefficient decreased with increasing heat flux and identified triangular wakes post-bubble nucleation. Their findings emphasised the role of vorticity and flow oscillations in heat transfer. Zhang et al. [34] tested silicon MPF with different pin sizes, achieving a maximum heat transfer coefficient of 60 kW/m<sup>2</sup>K. They found that pin density significantly affects performance and used an empirical model to explore trade-offs between electrical and thermal performance. Sarvey et al. [35] explored nonuniform MPF heat sinks for cooling integrated circuits with varying power densities. Clustering pin-fins over hotspots and spanning the channel width effectively reduced thermal resistance with a modest increase in pressure drop.

Furthermore, machine learning and artificial intelligence-related research is rapidly advancing in pin-finned heat sinks and thermal management for thermal and fluid flow predictions [36], performance enhancement [37], external validation [38], evaluation [39], design optimisation [40], temperature predictions [41], physics-informed neural networks (PINNs) [42], and Bayesian optimisation [43], amongst other applications [44–46]. However, the research focusing on micro pin-fins is limited. The flow characteristics from a macro to micro scale vary greatly depending on many external and physical factors. Nevertheless, some research in MPFHS and machine learning exists. For instance, Markal et al. [47] used machine learning to predict flow boiling behaviour in expanding type micro-pin-fin heat sinks (ETMPFHS). A new database with varying operational conditions was analysed using ML models, including Artificial Neural Networks (ANN), Support Vector Machine (SVM), Regression Trees (RT), and Linear Regression (LR). Results show that ANN is the most accurate for predicting heat transfer, temperature, and pressure, followed by SVM, while RT and LR were less effective.

Lee et al. [48] employed a Multimodal machine-learning approach, combining boiling pattern images with geometric and operational data, to predict heat transfer in micro-pin fin heat sinks. Among the four ML algorithms tested, the Multimodal model excelled, achieving high accuracy with a MAPE of 1.81 % for maximum temperature and 0.84 % for average temperature. Zhu et al. [49] found that the conventional machine learning model achieved good prediction accuracy with a 4.11 % deviation but was limited to the same data domain as its training data. By incorporating transfer learning, the model extended its applicability to new domains, achieving a similar accuracy with a 4.28 % deviation when using 70 % of new domain data. This demonstrates that transfer learning can effectively broaden the application range of machine learning models for predicting heat transfer in mini channels with micro pin fins.

Kim et al. [50] developed universal machine learning models to predict the thermal performance of micro-pin fin heat sinks with various geometries and operating conditions, surpassing the limitations of existing correlations. Using a database of 906 data points from 15 studies, the machine-learning models were compared with traditional regression models. The machine learning models achieved mean absolute errors (MAEs) of 7.5–10.9 %, significantly improving prediction accuracy by approximately fivefold compared to existing correlations. These models also demonstrated superior accuracy for rare geometric shapes and operating conditions, such as triangular pin shapes or using R134A as a working fluid, highlighting their effectiveness in predicting thermal performance across diverse scenarios.

As part of our literature scanning, the Scopus database showed that research on heat sinks has exponentially increased, totalling 29,184

publications over the past 25 years. Still, there is limited exploration combining heat sinks with "micro pin fin" technology (458 publications) and even fewer integrating "machine learning" (124 publications). Notably, only seven publications combined "micro pin fin" and "machine learning" in heat sink technology, indicating a significant research gap and opportunity for innovation and contribution. To get an overview of research trends, Fig. 1 shows a comparative visualisation graph of the research related to heat sinks and machine learning in the last 25 years.

Furthermore, although some nature-inspired pin-fin designs exist in different types of heat sinks [10,15,21,51], combining hybrid MFS with biomorphic or bio-inspired designs can significantly impact the design and efficiency of heat sinks; thus, it is an area that needs further investigation. The lack of substantial literature in these niche areas emphasises the need for focused and interdisciplinary research. Integrating technologies like MPF and machine learning into heat sink design could improve cooling efficiency for electronic devices and systems. Therefore, the potential findings of a combined strategy could strongly suggest a promising avenue for current and future investigations, impacting industries reliant on effective thermal management solutions.

Therefore, based on the discussed research gaps and literature findings, this research aims to advance the understanding and optimisation of micro pin-fin (MPF) heat sink technologies by designing and experimentally analysing four distinct biomorphic hybrid MPF geometries. Utilising an agile manufacturing approach, including a detachable and quickly reconfigurable heat sink setup with a 3D-printed case, the research seeks to explore various designs efficiently. By integrating experimental data with machine learning models, this research also endeavours to develop predictive tools and design strategies that enhance thermohydraulic performance across various high-demand applications, thereby contributing to academic knowledge and practical solutions. To achieve our research aim, we established a series of objectives. First, we designed and experimentally evaluated four innovative micro pin-fin (MPF) geometries to appraise their performance across important thermal metrics. Second, we investigated the impact of design shape and geometry on MPF performance to assess how the design variations influence overall heat transfer. Third, we created new empirical correlations for the best-performing hybrid biomorphic MPF

heat sink (MPFHHS) to predict the Nusselt number and pressure drops. Fourth, we analysed machine learning regression models using experimental data to evaluate the viability of predicting thermohydraulic performance in future heat sinks. Finally, we critically analysed insights from both experimental and machine learning models to propose optimised MPF-based thermal management solutions, all while incorporating an agile manufacturing philosophy throughout different stages of this research.

## 2. Experimental setup

The experimental setup, calibration, validation, uncertainty calculations, and equipment have been detailed in our previous research works [52,53]; therefore, it is described here briefly for brevity and to avoid repetition. In our previous and current study, we assessed the repeatability of key parameters such as pressure drop and Nusselt number across multiple test runs. The coefficient of variation for these parameters was under 4.8 %, indicating a good level of consistency in our measurements. Additionally, conducting experiments at two different power outputs enhanced the robustness of our results, demonstrating good repeatability even with varying heat fluxes, as the differences between the results were within acceptable ranges. The uncertainty associated with the experimental setup for Reynolds Number and Nusselt Number was under 7 % [53].

The setup involves a closed-loop flow circulation system suitable for single-phase and two-phase flows, designed to study heat transfer and flow dynamics in mini/microchannels and micro pin-fin-based heat sinks. Key components include a Masterflex gear pump (GJ-N23-PF1SA, UK), data loggers (Thermo Fisher Scientific DT80), a flow meter (Omega FTB332D-PVDF, USA), a pressure transducer (Omega PX2300, USA), a microscope (KERN OZM-5, Germany), thermal bath (Cole Palmer StableTemp Digital Bath, UK), and a 320 W power supply. A desktop computer was the base for setup initiation, control, and data storage. The DT80 data tracker monitored temperature distribution along the heat sink and system inlet/outlet while maintaining the water bath temperature. The experimental section was positioned horizontally, with the heat sink's temperature monitored by evenly spaced K-type thermocouples (RS-397-1589, UK) to prevent localised heating effects.

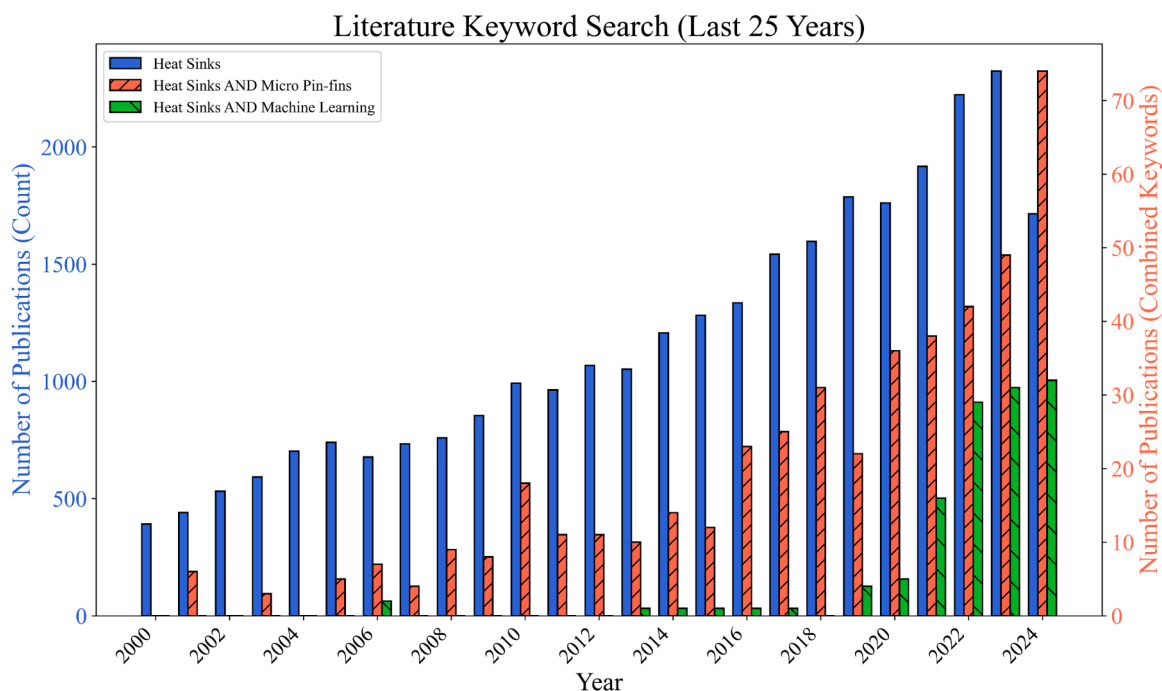


Fig. 1. Research trend of micro pin-fin heat sinks.

**Table 1**  
Experimental equipment range and accuracy.

Equipment	Model	Manufacturer (Country)	Range	Accuracy
Gear Pump	GJ-N23-PF1SA	MasterFlex (UK)	–	±0.1 %
Flow Meter	FTB332D-PVDF	Omega (USA)	0.1– 1 l/min	±6 %
Pressure Transducer	PX2300	Omega (USA)	0 – 1 PSID	±0.25 %
Power Supply	PS 2084–10B	Elektro-Automatik (Germany)	Voltage: 0 – 84 V Current: 0 – 10 A	<0.2 % <0.3 %
Thermocouples	RS-397–1589 (K-type)	RS Components (UK)	Temperature: –75 – 260 °C	±1.5 °C

Table 1 summarises the major equipment, range, and accuracy.

The flow originates from the thermal bath, which also serves as a storage tank. A gear pump circulates the working fluid—deionised water in this case—through the pipes to the experimental section (anticlockwise, from left to right). Along the way, the fluid passes through an electromagnetic flowmeter, where the flow rate is measured. A pressure transducer positioned behind the microscope records the pressure difference between the inlet (left port) and the outlet (right port). After passing through the experimental section, the fluid is cooled in an air-cooled radiator before returning to the thermal bath and then to the pump for recirculation, completing the closed-loop system. Fig. 2 shows the setup, instruments, and the schematic diagram for better understanding of the experimental setup’s working mechanism.

2.1. Wall temperature variations

To improve adaptability and ensure efficient changeovers in the experimental setup, a 3D-printed housing was created to encase the heat

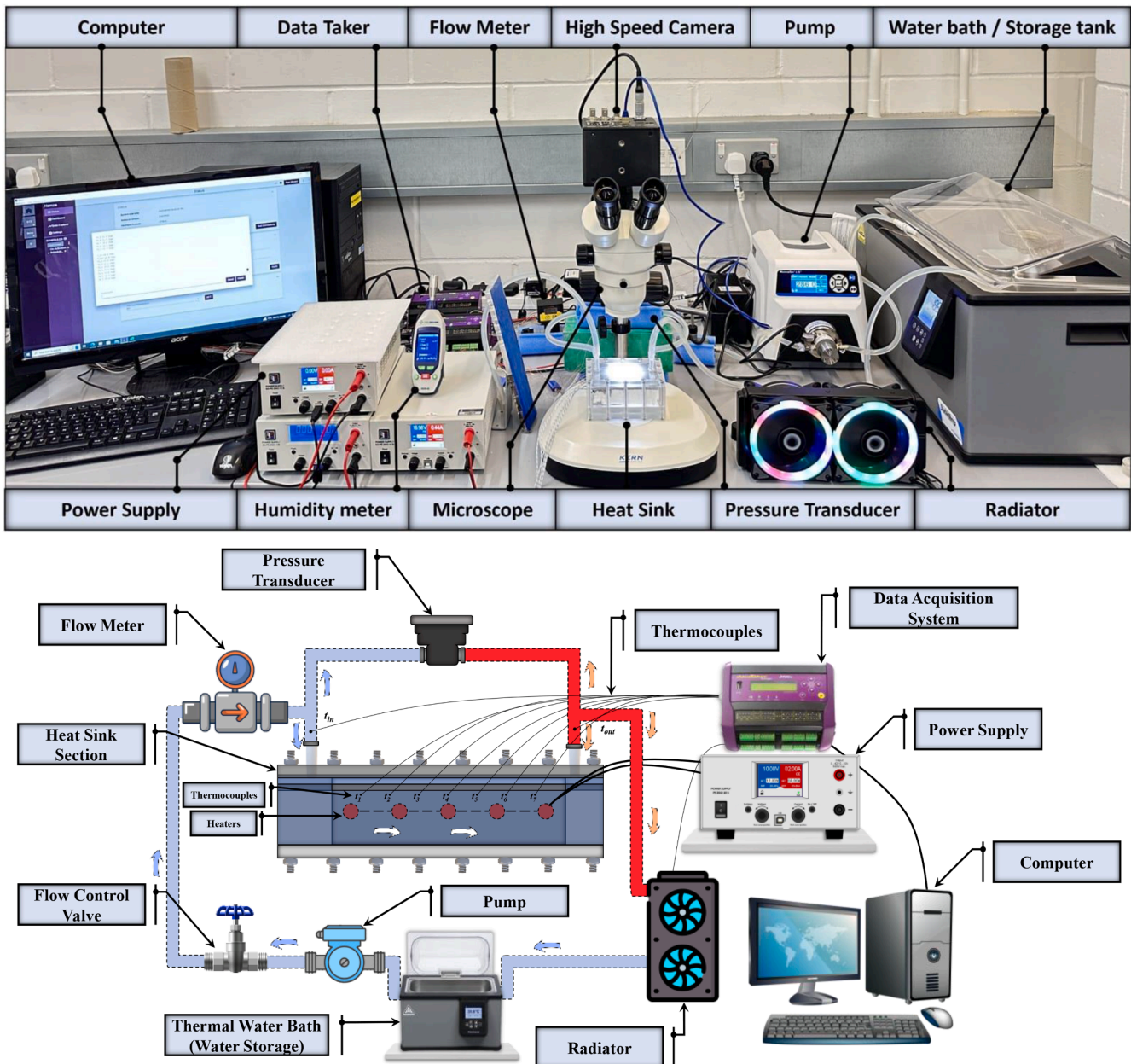


Fig. 2. Details of experimental setup.

sink/test section. The heat sinks were attached to a heating block equipped with six RSPro 300 W heaters along its length. RS PRO Non-Silicone Thermal Grease (4W/m·K) was applied at the contact interfaces to enhance heat transfer. Temperature measurements were taken using five K-type thermocouples placed equidistantly and parallel to the heating block, providing a detailed temperature profile. To assess the temperature distribution, any potential heat loss, and the impact of the thermal grease between the contact surface, an additional thermocouple was positioned 10 mm above the heating block to monitor the temperature at the centre of the heat sink wall that is attached to the heating block. The new 3D-printed casing (FormLabs Rigid 10 K resin, USA) allows for quick changeovers in single-phase flow, and it is also adaptable to high-temperature two-phase boiling conditions due to its high melting point of the resin (over 170 °C), heat deflection temperature at 0.45 MPa (218 °C), low thermal expansion coefficient (46 µm/m/°C for 0–150 °C), and ability to prevent heat loss due to low thermal conductivity (0.83 W/m·K). Given the resin’s thermal properties, temperature gradients between the fluid-solid interface and measurement points remain minimal, ensuring accurate readings without significant need for correction. For transient states, these material characteristics maintain stable temperature measurements, confirming negligible influence. Fig. 3 shows the modified experimental casing, while Fig. 3 shows the dimensions and details of thermocouple and heater placements.

The original acrylic setup was effective in minimising heat loss. Thus, due to the modification, one of the primary goals was to assess wall temperature differences and potential heat loss under various power outputs (100 W, 150 W, and 250 W) as the heating block was heated

from 20 °C to 100 °C under natural convection conditions; the dimension for the heating area is (80 mm x 60 mm). The average temperature across the heating block wall ( $T_{avg}$ ), measured by the five parallel thermocouples, as compared to the temperature at the centre of the heat sink wall ( $T_c$ ) recorded by the additional thermocouple. Results showed a temperature profile difference of 2 - 3 % between  $T_{avg}$  and  $T_c$  at all power levels. As we are using the  $T_{avg}$  for calculation of different thermal parameters, it was necessary to understand the effect of the thermal grease layer (between the heating block and the detachable heat sink) on the temperature difference; hence, the value of  $T_c$  was cross-checked to ensure the impact was minimal.

This slight 2–3 % variation can be attributed to several factors: the residual thermal resistance of the thermal paste, which, despite enhancing heat transfer, still presents a minor barrier; differences in thermocouple placement, with the embedded thermocouples and the external one under the heat sink experiencing slightly different thermal environments due to height variation; and the inherent measurement accuracy of the thermocouples, which typically have a margin of error of ±1.5 °C; this value encompasses both the inherent accuracy of the thermocouples, and the minor differences observed due to height variation between the embedded and external thermocouples and due to the effect of the thermal grease layer’s conductivity. The 2–3 % variation can be considered acceptable as it falls within the expected range of measurement uncertainty and does not significantly impact the overall thermal performance assessment. In terms of overall heat loss of the system from the housing, it varied between 11 % to 16.4 % for power outputs of 100 W, 150 W, and 250W. Fig. 4 shows the wall temperature distribution at different powers with times.

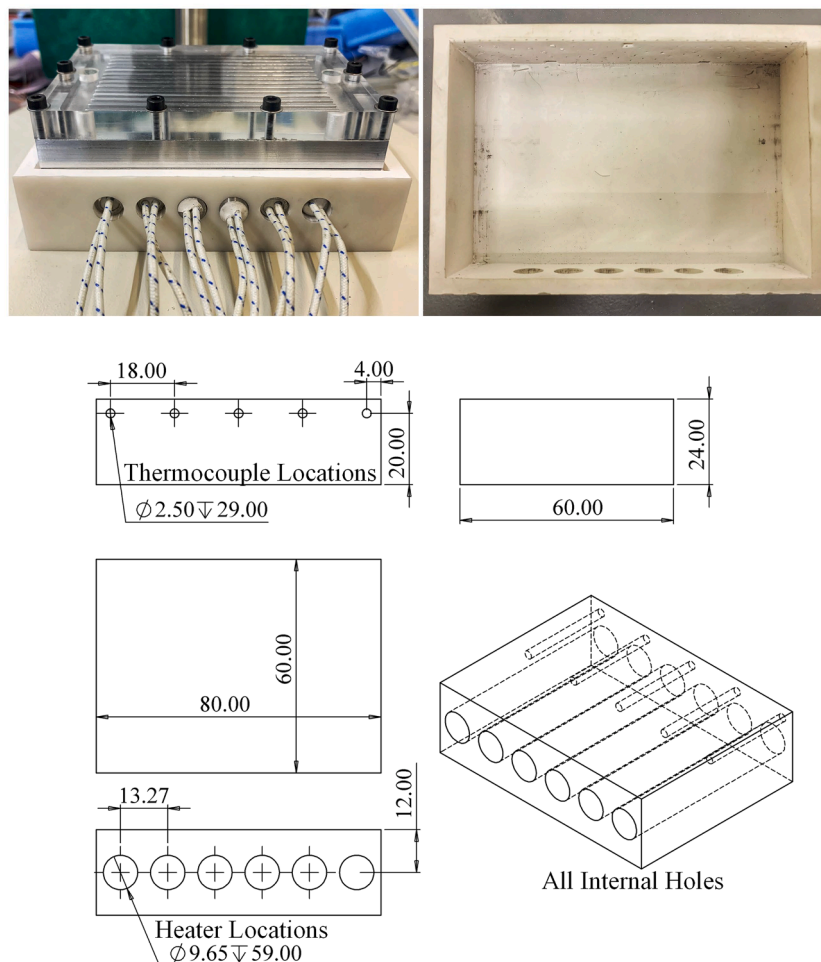


Fig. 3. Housing modification for a detachable heat sink setup.

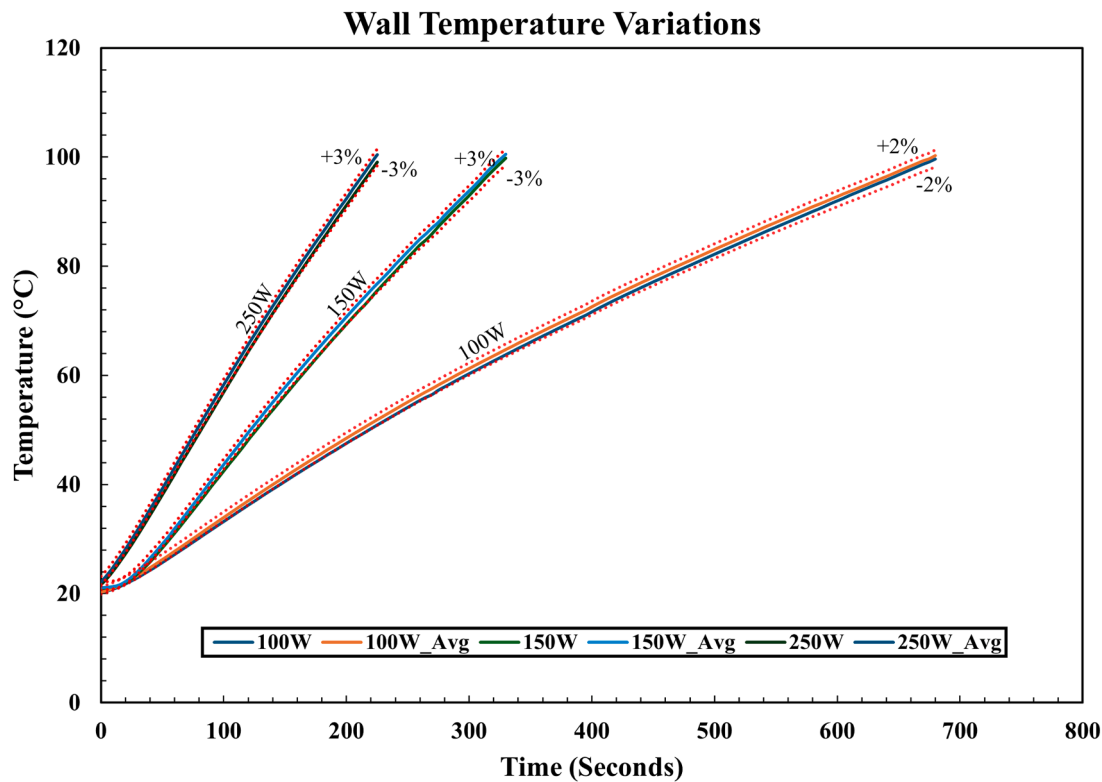


Fig. 4. Wall temperature variations for heating block and heat sinks.

Along with the adaptability benefits, the detachable setup promotes efficient material and component usage by allowing the same heating block to be used with different heat sink designs, enabling quick turn-over times when experimenting with various configurations. This flexibility is crucial for optimising thermal management solutions and enhances the efficiency of the experimental process — in alignment with the sustainable and agile manufacturing philosophy followed in this research. Moreover, by leveraging technologies such as additive manufacturing instead of traditional machining processes and 3D-printed resin instead of acrylic glass, this approach provides an alternative, effective, and sustainable method for experimenting with thermal management and heat dissipation in electronic and mechanical systems, ensuring reliable performance under varied operating conditions.

### 3. Heat sink designs, rationale, and manufacturing

In this study, four distinct biomorphic micro pin-fin heat sink designs were developed and manufactured. Each design was inspired by biological forms and tailored to optimise thermal performance by enhancing flow dynamics and mixing. By manipulating thermohydrodynamic properties such as turbulence, thermal resistance, and heat transfer efficiency, these designs aim to improve the overall thermohydraulic performance of the heat sinks. The key features and underlying thermohydrodynamic/thermohydraulic rationale for each design are detailed below.

#### 3.1. Cruciform flower-inspired designs

**Cruciform Flower with Astroid Splitters (CFAS):** The first design features a cruciform flower pattern, characterised by a cross-shaped configuration at the centre of the heat sink. To enhance flow mixing and redistribution, petal-shaped and astroid-shaped splitters are integrated between the cruciform sections. These splitters are strategically placed to redirect the coolant flow into the surrounding pin-fin sections.

From a thermohydrodynamic perspective, the design intends to:

- **Increase Turbulence:** By introducing obstructions in the flow path, the splitters induce turbulence, disrupting the laminar boundary layer and enhancing convective heat transfer;
- **Enhance Mixing:** The splitters promote coolant mixing, leading to a more uniform temperature distribution and reducing thermal resistance;
- **Optimise Flow Distribution:** Redirecting the flow ensures that all pin-fin surfaces are effectively utilised, preventing hotspots and improving overall heat transfer efficiency.

This design aims to balance flow distribution and mixing efficiency, potentially improving the interaction between flow redirection and pin-fin cooling surfaces to improve thermal performance.

**Cruciform Flower with Secondary Microchannels (CFSM):** Building upon the cruciform flower shape, the second design omits the astroid splitters. The absence of splitters allows the gaps between the cruciform sections to act as secondary microchannels, providing additional and unrestricted pathways for coolant flow. Thermohydraulic considerations for this design include:

- **Reduced Pressure Drop:** The open microchannels decrease flow resistance, lowering the overall system pressure drop compared to designs with flow obstructions;
- **Laminar Flow Maintenance:** The additional channels may promote laminar flow conditions, which can be beneficial for certain operating regimes;
- **Optimised Flow Distribution:** The secondary lanes facilitate more uniform coolant distribution, potentially enhancing thermal performance by ensuring consistent cooling across the heat sink.

This configuration is designed to evaluate the effect of secondary flow lanes on overall system pressure drop and heat transfer, aiming to find an optimal balance between enhanced mixing and effective flow

distribution, as previous literature has reported potential benefits of having secondary lanes.

### 3.2. Exocoetidae-inspired designs

**Exocoetidae-Inspired Shape with Sharp Edges (ESE):** The third design draws inspiration from the morphology of Exocoetidae (flying fish), with pin fins shaped to emulate this natural form. Key features include: 1) Hexagonal Base: each pin fin has a hexagonal base, a shape known to offer favourable thermal performance due to its increased surface area and ability to induce turbulence; 2) Kite or Diamond-Shaped Fins: extending from the base are fins reminiscent of wings, serving to compress and expand the coolant flow, enhancing mixing and promoting turbulent flow; 3) Trapezoidal Tail: designed to expand the flow further, ensuring effective utilisation of all pin fins and minimising areas of stagnant flow; 4) Interspersed Circular Pin Fins: placed between the kite-shaped fins, these contribute to additional flow mixing by forming continuous expansion and convergence zones. Thermohydrodynamic rationale includes:

- **Controlled Flow Expansion and Compression:** By manipulating the flow pathways, the design increases turbulence intensity, disrupting thermal boundary layers and enhancing convective heat transfer coefficients;
- **Maximised Surface Area:** The complex geometry increases the contact area between the coolant and the heat sink, reducing thermal resistance;

- **Enhanced Turbulence:** Sharp edges and abrupt changes in flow direction induce turbulence, potentially improving heat transfer; albeit, pressure may also increase.

This design focuses on leveraging complex geometry to optimise thermal management by controlling flow expansion, convergence, and mixing.

**Exocoetidae-Inspired Shape with Filleted Edges (EFE):** Retaining the overall geometry of the third design, the fourth design introduces filleted edges to the pin fins instead of sharp edges. From a thermohydraulic and thermohydrodynamic performance consideration, the filleted-edged designs are intended to:

- **Reduce Flow Resistance:** Streamlining the geometry decreases pressure drop across the heat sink by minimising frictional losses;
- **Alter Turbulence Levels:** Smoother edges may reduce turbulence intensity, potentially lower levels of turbulence;
- **Improve Thermal Efficiency:** By decreasing flow resistance, the coolant can flow more freely, which may enhance heat transfer efficiency under certain conditions;
- **Balance Between Turbulence and Pressure Drop:** The design seeks to maintain sufficient turbulence for effective heat transfer while reducing the pressure losses associated with high turbulence levels;
- **Thermal Resistance Reduction:** Smoother flow paths may lower thermal resistance by facilitating more efficient heat exchange between the coolant and heat sink surfaces.

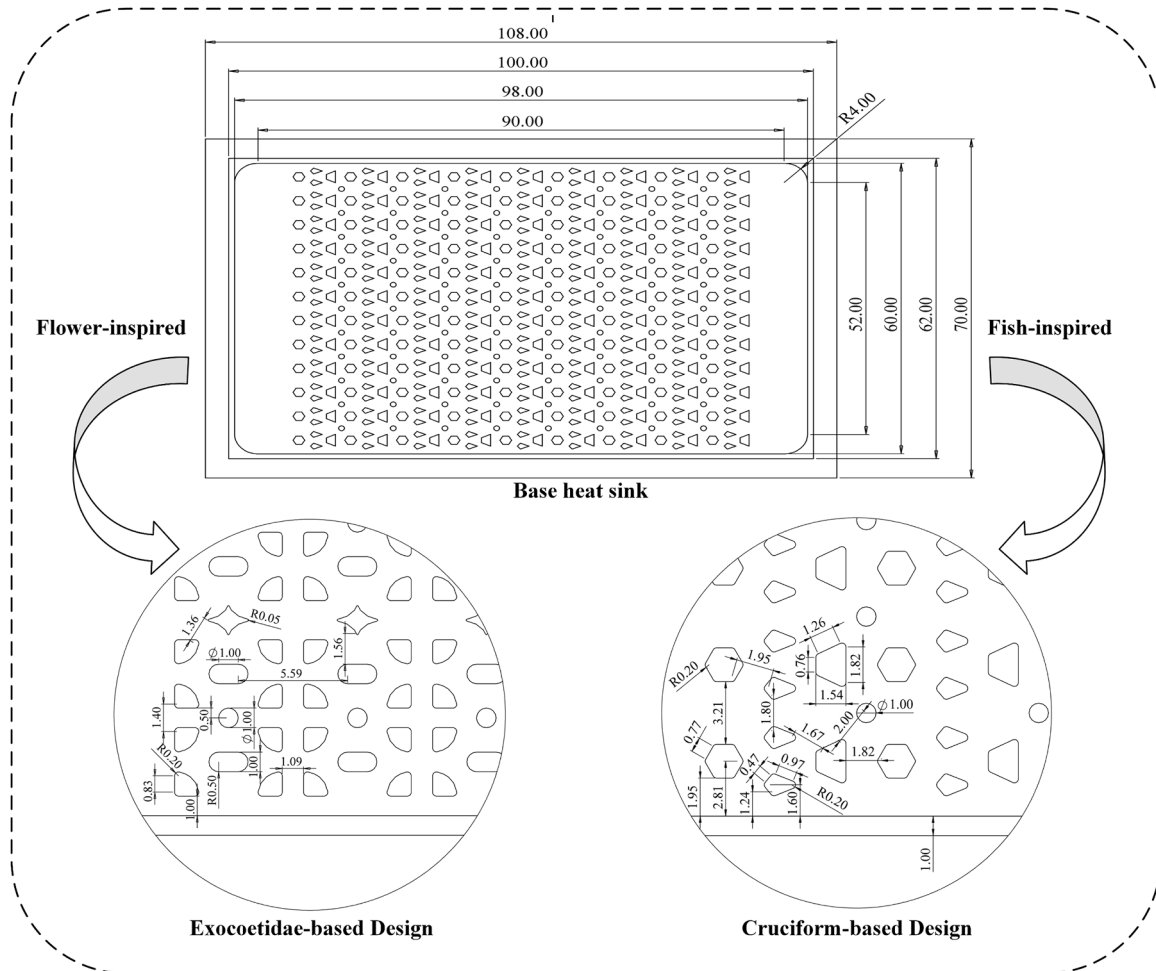


Fig. 5. Pin-fin dimensions and drawing.



By comparing the ESE and EFE designs, the study assesses the impact of edge geometry on flow dynamics and thermal performance, aiming to find an optimal balance between enhanced mixing and reduced flow resistance.

Fig. 5 shows the drawing and dimensions of the pin-fins. Note that all the heat sinks have the same base dimensions and cover the same effective heating area (80 mm × 60 mm); therefore, for the purpose of brevity, ESE design is shown as the base design.

### 3.3. Overview of design features and rationale

By incorporating innovative geometric elements such as astroid splitters, microchannels, and filleted edges, these designs contribute to a deeper understanding of how biomorphic-inspired hybrid pin-fin heat sink geometries can be utilised to advance thermal management in microelectronic systems. Table 2 shows the key design features of the four heat sinks. The pin fins were designed in segments and distributed in equidistant rows and columns to ensure uniform flow distribution and thermal performance. The height of each pin-fin was 1mm. Fig. 6 provides an overview of the design rationale and the final manufactured micro pin-fin heat sinks (MPFHS).

### 3.4. Agile manufacturing philosophy in micro-pin fin development

Practical and cost constraints influenced the manufacturing of the heat sinks; therefore, they were produced using 3-axis CNC milling. Tolerance control was a primary consideration. While a tolerance of 0.05 mm was readily achievable, tightening it to 0.01 mm posed significant challenges, leading to exponential cost increases. Therefore, the design prioritised fin spacing and hole dimensions that directly impact manufacturability and performance, rather than tightest tolerances.

**Fin spacing and height considerations:** Fin spacing and height were critical design factors. With a 1 mm spacing and 1 mm fin height, the milling process divides the height into 20 layers, each milled at a depth of 0.05 mm. Reducing fin spacing to 0.5 mm requires the milling tool to make twice as many passes per layer, effectively doubling processing time and cost. The narrower spacing necessitates more frequent, controlled passes because the tool must remove material in smaller increments to prevent damage to the adjacent fin walls. This process adds layers or steps, ensuring accuracy and maintaining the structural integrity of each fin. Further reduction to 0.1 mm spacing can exceed equipment capabilities, making machining unfeasible due to increased time and expense — also going against agile philosophy.

**Hole processing constraints:** Hole processing constraints also influenced the design. The length-diameter ratio (hole length divided by diameter) is critical for machining ease. Holes with a ratio less than 8 are

relatively easy to machine, but as this ratio increases, processing difficulty and cost rise exponentially. For very small holes (e.g., 0.5 mm diameter), the acceptable ratio becomes even more restrictive. These considerations ensured holes remained within manageable ranges for cost-effective manufacturability.

**Inline vs staggered configuration:** To further optimise manufacturing efficiency and reduce costs, the micro pin-fins were arranged inline rather than staggered. For non-conventional pin-fins, inline configurations can yield better results [54]. Inline arrangements simplify milling paths, reducing tool movement complexity, machining time, and required passes. In contrast, staggered configurations demand more complex paths and additional passes, increasing time and cost. Inline setups also streamline machine alignment, making the process more efficient. Overall, inline designs reduce processing time, complexity, costs and keeps production within budget.

**Integration with agile manufacturing concepts:** Machining constraints were integral to the design strategy, aligning with agile manufacturing principles that emphasise flexibility, rapid prototyping, and iterative design [55]. Understanding the exponential cost implications of tight tolerances, reduced fin spacing, inline configurations, and challenging hole dimensions allowed the design to optimise key parameters for performance without excessive cost and time. Choosing a 3-axis milling process enabled rapid prototyping and testing of different iterations, quickly identifying feasible designs balancing performance and manufacturability. In summary, agile manufacturing concepts shaped the final heat sink designs by iteratively refining within practical constraints, achieving a balance between innovative geometry, thermal efficiency, and manufacturability. This approach optimised production, ensuring the final products could be produced timely, cost-effectively, and meet performance requirements.

**Surface Morphology:** The scanning electron microscope (SEM) images and 3D depth map reveal a channel and height variations up to 646.78  $\mu\text{m}$ , featuring consistent grooves typical of micro heat sink fabrication due to micro-machining limitations and cost-efficiency needs; the surface had roughness of 0.8 to 1.6  $\mu\text{m}$ . While the SEM image shows surface textures and grooves, the 3D depth map provides a broader view, highlighting the overall height variations across the surface. The average surface channel depth of around 300–400  $\mu\text{m}$  indicates a fairly consistent topography. This structured roughness can enhance heat transfer by promoting micro-turbulence, while the high surface homogeneity ensures minimal variation to flow and thermal performance. Importantly, the texture affects surface interactions without impacting the material's thermal conductivity, preserving overall heat sink efficiency [56]. Therefore, aiming for an improved surface finish is neither a necessary nor cost-effective strategy, as the existing texture effectively supports the design's thermal performance requirements. Fig. 7(a) and (b) shows the surface characteristics.

**Table 2**  
Summary of key design feature details.

Design	PF Segments	Total No. of PFs	Geometry Type	Interreuptor	PF Area (mm <sup>2</sup> )
EFE	108 (12 × 9)	520	Hexagon, Kite, Trapezoid (0.2 mm filleted edges)	Cylindrical (1mm) Total = 88 (11 × 8)	2468
ESE	108 (12 × 9)	520	Hexagon, Kite, Trapezoid (no fillets)	Cylindrical (1mm) Total = 88 (11 × 8)	2675
CFSM	72 (12 × 6)	792	Curved Arcs;(90° angled segments); petaloid rectangles	Secondary lanes (2mm) Total = 5 (5 × 1)	3122
CFAS	72 (12 × 6)	852	Curved Arcs (90° angled segments); petaloid rectangles	Astroid ( $\sqrt{2}$ mm) Total = 60 (12 × 5)	3410

## 4. Data reduction

During the experimental run, data was recorded at timed intervals to examine the thermal performance of single-phase heat transfer. The recorded data included the inlet and outlet temperatures of the deionised water as a working fluid, along with temperatures at five equally spaced points within the heat sink. Parameters such as flow rate, pressure drop, and heat dissipation were also monitored. Additionally, various equations were employed to study the experimental results, enabling the calculation of crucial performance parameters related to heat transfer and thermal characteristics, including thermal resistance, Reynolds number, Nusselt number, and pressure drops. As mentioned in the earlier section, the test section was well insulated to minimise heat loss, therefore adapting previous works [10,53,57,58], the baseline governing equations for data reduction were as follows:

Convective heat transfer rate (Q):

$$Q = m\dot{c}_p(T_{out} - T_{in}) \quad (1)$$

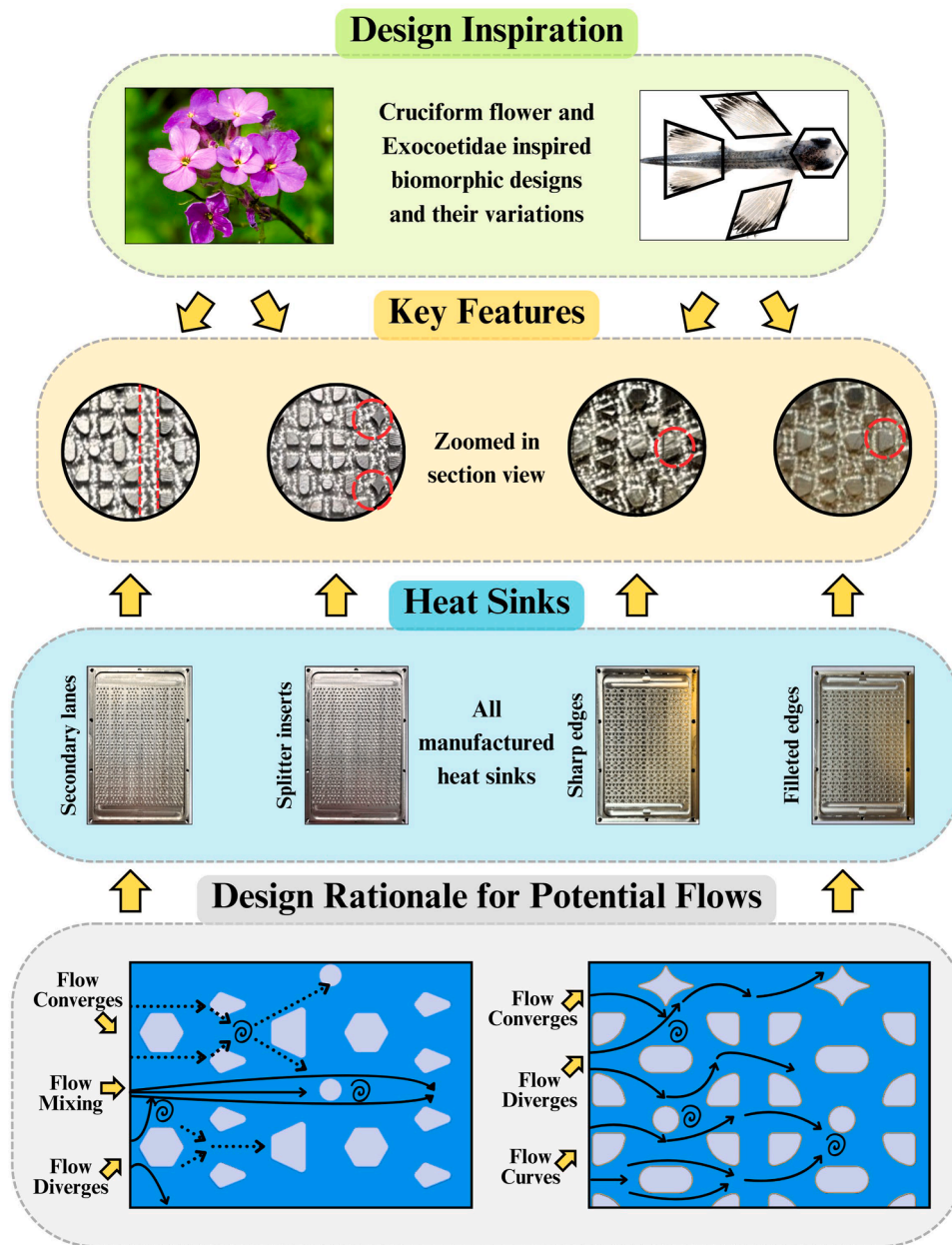


Fig. 6. Heat sink designs and inspirations.

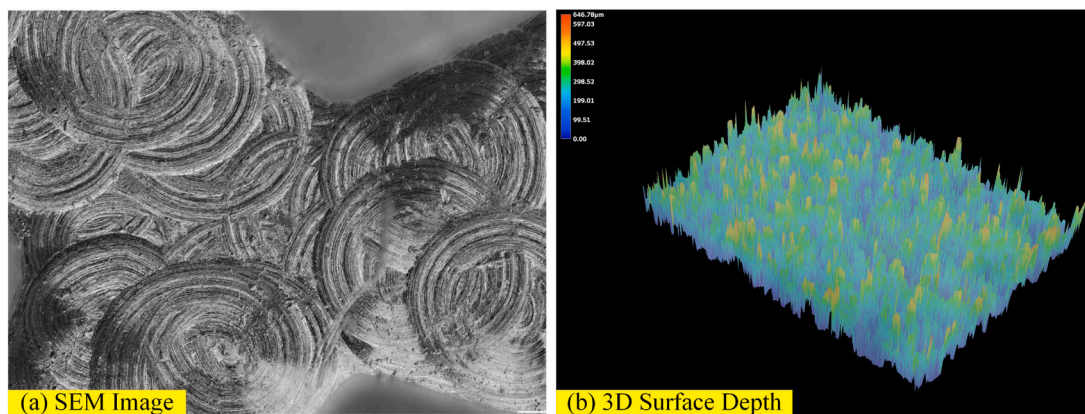


Fig. 7. (a) SEM Image, (b) 3D Surface Depth.

where  $T_{in}$  and  $T_{out}$ ,  $\dot{m}$  and  $c_p$  refers to the inlet and outlet temperature, mass flow rate, and coolant's specific heat capacity respectively

To calculate density, specific heat, and viscosity, the mean fluid temperature ( $T_m$ ) is given by:

$$T_m = \left( \frac{T_{in} + T_{out}}{2} \right) \quad (2)$$

Although the current designs have some degree of developing flow due to the inlet entrance, Eq. (2) provides reliable calculations with minimal errors, as highlighted in past research [54,57,59].

Characteristics Length ( $L$ ) or Hydraulic diameter ( $D_h$ ):

$$L = D_h = \frac{4A}{P} \quad (3)$$

where  $A$  is the cross-section area and  $P$  is the perimeter of the inlet area available for flow and exposed to the pin fins.

Reynolds Number ( $Re$ ):

$$Re = \frac{\rho v L}{\mu} \quad (4)$$

where  $\rho$ ,  $v$ ,  $\mu$  are fluid density, velocity, and viscosity, respectively

Wall Temperature ( $T_w$ ):

$$T_w = T_b - \left( \frac{Q L_x}{k_s A_w} \right) \quad (5)$$

$$A_w = L_{ts} \times W_{ts} \quad (6)$$

where  $T_b$  temperature below the channel wall (cw);  $L_x$  is the distance from the base to cw;  $k_s$  is the thermal conductivity of the heat sink;  $A_w$  is the surface area of the cw given as a product of the length ( $L_{ts}$ ) and width ( $W_{ts}$ ) of the test section covered by the pin fins within the heat sink.

The logarithmic mean temperature difference (LMTD):

$$LMTD = \frac{(T_w - T_{in}) - (T_w - T_{out})}{\ln \left[ \frac{(T_w - T_{in})}{(T_w - T_{out})} \right]} \quad (7)$$

The LMTD approach provides a representative average driving force for heat transfer across the length of the heat sink, capturing the effects of this temperature variation more accurately than a constant wall-to-fluid temperature difference.

Effective fin area ( $A_{eff}$ ):

$$A_{eff} = N A_f H_f + A_w \quad (8)$$

where  $N$  is the number of fins or fin sections

Convective heat transfer coefficient ( $h$ )

$$h = \frac{Q}{A_{eff} \times LMTD} \quad (9)$$

Nusselt Number ( $Nu$ )

$$Nu = \frac{h \times D_h}{k_f} \quad (10)$$

where  $k_f$  is the thermal conductivity of the fluid

Thermal Resistance ( $R_{th}$ ):

$$R_{th} = \frac{LMTD}{Q} \quad (11)$$

Pressure drops ( $\Delta P$ ):

$$\Delta P = (P_{inlet} - P_{outlet}) \quad (12)$$

Pumping Power Usage ( $P_u$ ):

$$P_u = \frac{\Delta P \times \dot{m}}{\rho} \quad (13)$$

## 5. Results

### 5.1. Nusselt number

The Nusselt number ( $Nu$ ) is an important dimensionless parameter that helps to quantify convective heat transfer between fluid and solid surfaces.  $Nu$  varies with fluid flow conditions, providing insights into fluid behaviour. When  $Nu$  equals 1, heat transfer by conduction equals that by convection.  $Nu$  values of  $>1$  imply more efficient heat transfer by convection, highlighting effective cooling mechanisms. The study evaluated the heat transfer efficiency of four micro pin-fin heat sink designs — EFE, ESE, CFMS, CFAS — by calculating their Nusselt numbers ( $Nu$ ) across Reynolds numbers ( $Re$ ) ranging from 101 to 507, with a power output of 150 W and 250W. Fig. 8(a)-(d) shows the  $Nu$  performance of the designs.

Looking at Fig. 8(a) and 8(b), the results show that the filleted design (EFE) steadily increased in Nusselt number from 8.4 to 8.9 at  $Re$  101 to a maximum of 12.4–12.9 at  $Re$  507, indicating improved heat transfer efficiency with higher flow velocities. However, the overall  $Nu$  values at 250 W are around 4–5 % lower than at 150W. In comparison, the edged design (ESE) shows a more moderate increase in Nusselt number, from 7.6 to 7.9 at  $Re$  101 to 9.6–10.2 at  $Re$  507, suggesting that the sharp edges provide less significant improvement in heat transfer compared to the filleted design. For ESE, the overall  $Nu$  is also lower at 250 W than 150W.

The CFMS design demonstrated the lowest Nusselt numbers, increasing from 5.2 to 5.3 at  $Re$  101 to 8.0–9.1 at  $Re$  507, indicating lower effectiveness in enhancing heat transfer. For CFMS, the heat transfer efficiency shows a different trend than other designs, with the overall  $Nu$  being more effective at 250 W than 150W. The CFAS design, featuring astroid splitters, achieves the second-highest  $Nu$  overall and the highest  $Nu$  at lower  $Re$  values, ranging from 8.8 to 9.8 at  $Re$  101. At max  $Re$  value, the  $Nu$  ranges from 12.1 to 12.5 at  $Re$  507, indicating superior heat transfer performance relative to the two other designs. As observed with the other two designs, the heat transfer efficiency is slightly better at 150 W than at 250W.

Overall, across both power outputs, the EFE and CFAS designs consistently demonstrated the highest Nusselt numbers, confirming them as the most efficient designs for heat transfer. The CFAS design performs well initially but shows signs of a gradual decrease in heat transfer efficiency at higher Reynolds numbers and power outputs. The ESE design provides moderate performance with steady but limited improvements, while the CFMS design is the least effective.

To further evaluate the performance of the new designs, the Nusselt number ( $Nu$ ) results of the two best-performing designs at 150 W were compared with those reported in the existing literature, as shown in Fig. 8(c). Also, to gain a more comprehensive understanding, different setup strategies were considered. For instance, Ali and Arshad [57] examined conventional square pin fins arranged in inline and staggered configurations using both water and nanofluids. Their experiments were conducted at a power output of 192 W within a Reynolds number ( $Re$ ) range similar to this study. However, since this current research focused on an inline configuration and did not involve nanofluids, the first comparison was limited to their inline square fin setup with water as the working fluid. The second study considered micro pin fins from the research of Ambreen and Kim [59], who experimented with hexagonal pin fins—a key feature of ESE and EFE designs—and conducted within a  $Re$  range of 250 to 550. However, because they did not provide  $Nu$  performance values using water, their use of nanofluids for performance enhancement was taken as an additional basis for comparison.

Moreover, Chai et al. [60] investigated a three-dimensional numerical model of a non-conventional interrupted microchannel heat sink with mixed geometries. They explored the effects of pressure drop and heat transfer characteristics resulting from various dimensions and positions of rectangular ribs within transverse microchambers. Although

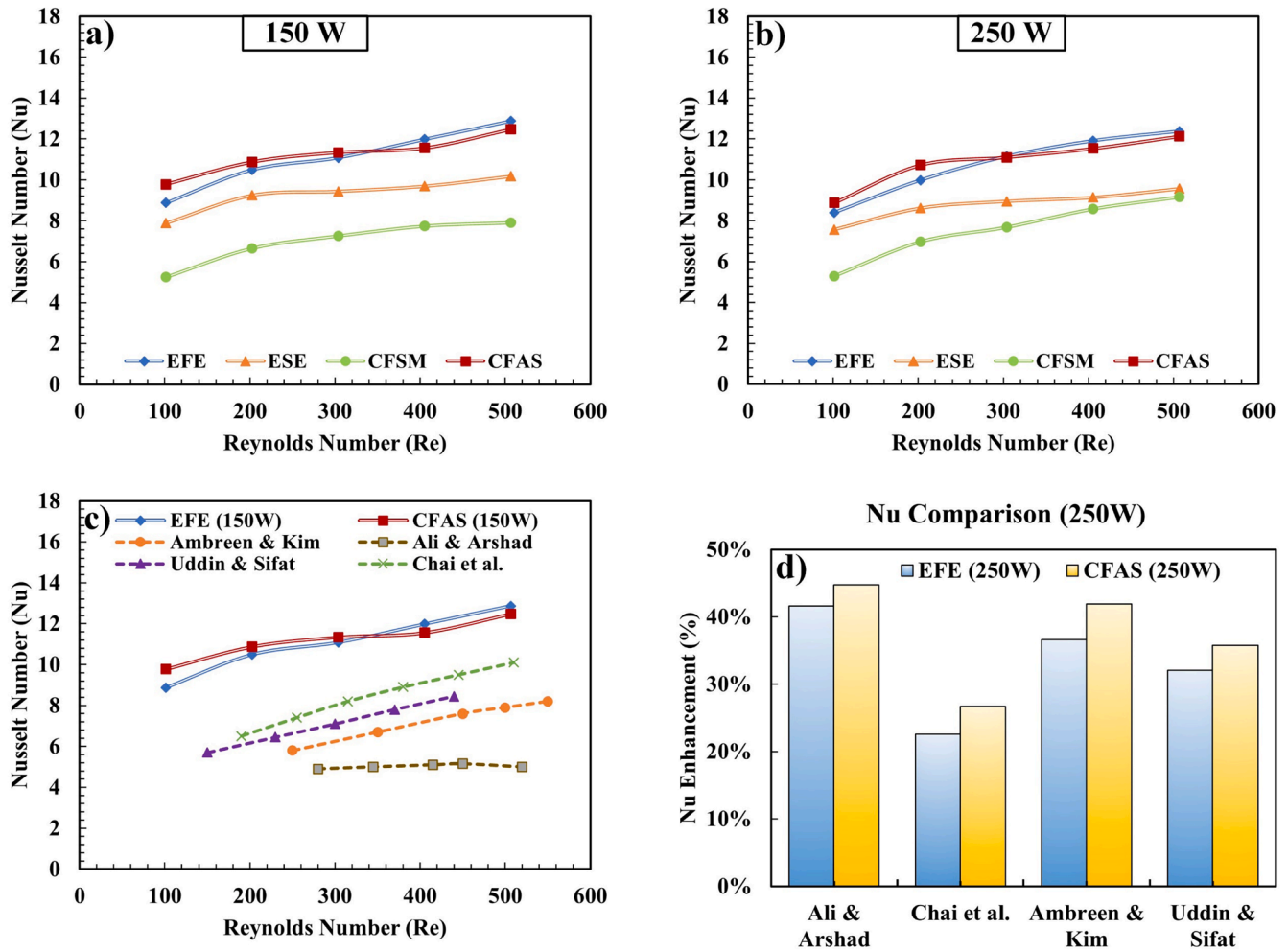


Fig. 8. (a)-(d) Nusselt Number comparison.

their research focused on microchannels, the presence of interrupted and varied geometries makes it a valuable basis for comparison with this study. Additionally, the mixed geometry with interruptions in Chai et al.'s [60] design can be appraised against the new designs, which also feature mixed geometry with asteroid splitters/cylindrical interrupters. Lastly, Uddin and Sifat [61] analysed the thermo-hydraulic characteristics of Mini-Channel Heat Sinks (MnCHS) featuring different secondary channel shapes—rectangular, oblique, and curvy—across a  $Re$  range of 150 to 1050; however, for a more like-for-like comparison, their  $Re$  values will be limited to 550 as the current research investigates  $Re$  values between 100 and 500. In summary, the four studies with comparable strategies implemented in various types of heat sink setups provided a solid foundation for performance evaluation.

Additionally, to focus on both the maximum and minimum performances, Fig. 8(d) shows the performance comparison of the EFE and CFAS designs with those from extant literature at the lowest Reynolds number (requiring the least pumping power) at 250W. The key findings were:

- **EFE Design:** The EFE design shows a significant enhancement in performance, with improvements ranging from 23 % to 42 % over the designs presented in the literature. The highest enhancement (42 %) is observed when compared with the design by Ali & Arshad, suggesting that the design offers substantially better heat transfer efficiency. Additionally, when comparing at the highest  $Re$  Number and pumping power, the EFE and CFAS designs show over 140 % Nu enhancement compared to the inline rectangular pin-fins of Ali &

Arshad. Even the lowest enhancement of 23 % against Chai et al. [60] still represents a meaningful improvement, highlighting the efficacy of the EFE design.

- **CFAS Design:** At lower  $Re$ , the CFAS design performs slightly better than the EFE design, with enhancements ranging from 27 % to 45 % compared to the literature. The maximum improvement of 45 % over Ali & Arshad demonstrates that the CFAS design is particularly effective, likely due to its ability to manage fluid flow and surface interaction more efficiently. The lowest improvement of 27 % against Chai et al. [60] still exceeds the performance, reaffirming the superior performance of the CFAS configuration.

The performance comparison with existing literature indicates that the EFE and CFAS designs developed in this study offer substantial enhancements in Nusselt number at 250 W compared to previously reported designs. The CFAS design, in particular, outperforms the EFE design at lower  $Re$ , but the EFE design outperforms CFAS overall, making it the most effective in enhancing heat transfer efficiency. This comparative analysis further validates the effectiveness of these innovative heat sink designs and suggests that they could offer significant advantages in practical applications where efficient thermal management is critical.

### 5.2. Thermal resistance

Thermal resistance, a key factor in heat transfer analysis, defines the resistance a system presents to heat flow. Reducing thermal resistance is

crucial for improving heat transfer efficiency and ensuring electronic devices and other heat-generating systems operate safely. This study measured thermal resistance across different heat sink designs—EFE, ESE, CFSM, and CFAS—under various flow rates (Reynolds numbers) and heating powers (150 W and 250 W). Fig. 9(a)-(b) shows the thermal resistance trend for 150 W and 250W.

As anticipated, thermal resistance generally decreased with increasing Reynolds numbers, signifying enhanced heat dissipation at higher flow rates. At 150 W, the CFAS design consistently exhibited the lowest thermal resistance, recording a minimum value of 0.0333 K/W at  $Re = 507$ . This superior performance can be attributed to the CFAS design's optimised surface area and fluid flow channels, which likely promote more effective heat transfer. In contrast, the CFSM design showed the highest thermal resistance, reaching 0.0821 K/W at  $Re = 101$ . The higher resistance in CFSM could be due to less efficient fluid flow patterns, leading to reduced surface heat removal.

The EFE and ESE designs displayed thermal resistance values between CFAS and CFSM data, with EFE generally outperforming ESE. This suggests that the EFE design may have better thermal contact or more favourable flow characteristics than ESE, though not as optimised as CFAS.

At 250 W, a similar pattern was observed: CFAS continued to outperform the other designs, achieving a thermal resistance of 0.0343 K/W at  $Re = 507$ , while CFSM again showed the highest resistance, especially at lower flow rates, with 0.0815 K/W at  $Re = 101$ . The slightly higher thermal resistance across all designs at 250 W compared to 150 W could be due to the increased heat load, which might exacerbate the inefficiencies in heat transfer, particularly in designs like CFSM.

The results highlight that among the tested configurations, CFAS is the most effective in minimising thermal resistance, particularly at higher flow rates. This efficiency likely stems from its design, which facilitates better fluid distribution and heat removal. Conversely, the CFSM design's higher thermal resistance suggests potential areas for improvement in its thermal management strategy, such as enhancing flow uniformity or increasing surface area contact.

The apparent dependence of thermal resistance on heat input ( $Q$ ) in the pin-fin heat sinks likely results from slight temperature-induced variations in fluid properties, which can affect convective heat transfer. Additionally, some effect arises from the thermal properties of the thermal grease layer used, as its conductivity and thickness can influence overall thermal resistance, particularly at higher heat fluxes. Regarding the potential for mixed convection, we calculated the Grashof and Rayleigh numbers and found them to be relatively low, indicating that natural convection effects were negligible in our single-phase flow setup. Consequently, mixed convection was not a contributing factor, and the system remains governed by forced convection.

### 5.3. Pressure drop and energy consumption

In the design and evaluation of heat sinks, understanding pressure drop values, pumping power requirements, and energy consumption is essential for optimising performance and operational costs. Pressure drop measures the resistance to fluid flow through the heat sink, which affects the amount of pumping power needed to maintain adequate coolant circulation. Higher pressure drops usually result in greater energy consumption, influencing the overall efficiency and cost-effectiveness of the cooling system. Thus, balancing these trade-off factors is important for selecting the most appropriate heat sink design for a given application.

The analysis of heat sink designs—EFE, ESE, CFSM, and CFAS—was conducted at both 150 W and 250 W heating powers. Fig. 10(a)-(d) presents the data related to pressure drops and associated parameters. Although the values were assessed for both power outputs, the differences between them were minimal, as seen from Fig. 10(a) and 10(b), so the results primarily focus on the higher heat flux/power output of 250 W data for clarity and brevity purposes.

The ESE design, with sharp-edged micro pin-fins, demonstrates the second highest pressure drop among the designs, measuring 350.6 Pa at  $Re = 101$  and reaching 4001 Pa at  $Re = 507$ . This significant resistance to fluid flow translates into a high pumping power requirement of 60.1 mW. Consequently, the ESE design has one of the lowest energy efficiencies, consuming 1 kWh of energy in 692.8 days. The sharp edges create substantial turbulence and flow disruption, potentially leading to increased pressure drop and operational costs.

Conversely, the CFSM design features a secondary flow lane between the pin fins, which helps to alleviate some of the flow resistance. This results in a moderate pressure drop of 220 Pa at  $Re = 101$  and 3340 Pa at  $Re = 507$ . Despite this moderate pressure drop, the CFSM design requires a lower pumping power of 50.2 mW. It demonstrates the longest energy consumption time of 830.3 days for 1 kWh, indicating better overall energy efficiency.

The EFE and CFAS designs excel in heat transfer performance, as indicated by their high Nusselt numbers ( $Nu$ ). The EFE design, with its curved filleted edges, achieves a pressure drop of 160 Pa at  $Re = 101$  and 3463 Pa at  $Re = 507$ . This design strikes a balance by minimising flow separation and turbulence, requiring 52 mW of pumping power and consuming 1 kWh of energy in 800.6 days. The energy consumption is relatively low, considering its effective thermal performance. Similarly, the CFAS design incorporates splitter inserts between the flow lanes to enhance heat transfer efficiency. However, this design leads to the highest pressure drop of 216 Pa at  $Re = 101$  and 4224 Pa at  $Re = 507$ . It requires 63.5 W of pumping power and consumes 1 kWh of energy in 656.3 days. Although CFAS shows a higher resistance compared to EFE,

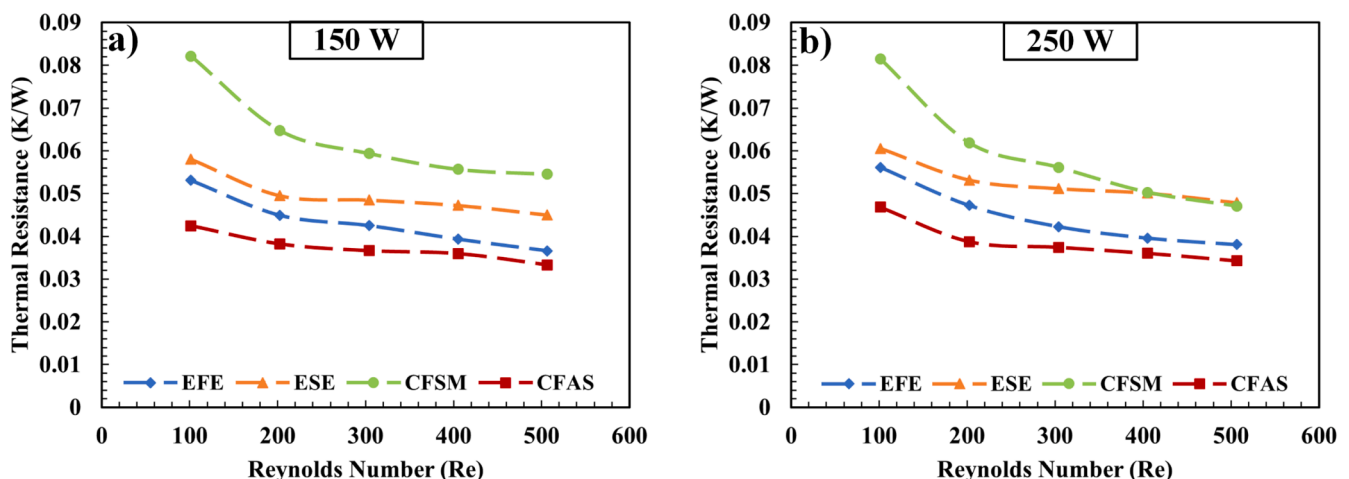


Fig. 9. (a)-(b) Thermal resistance performance.

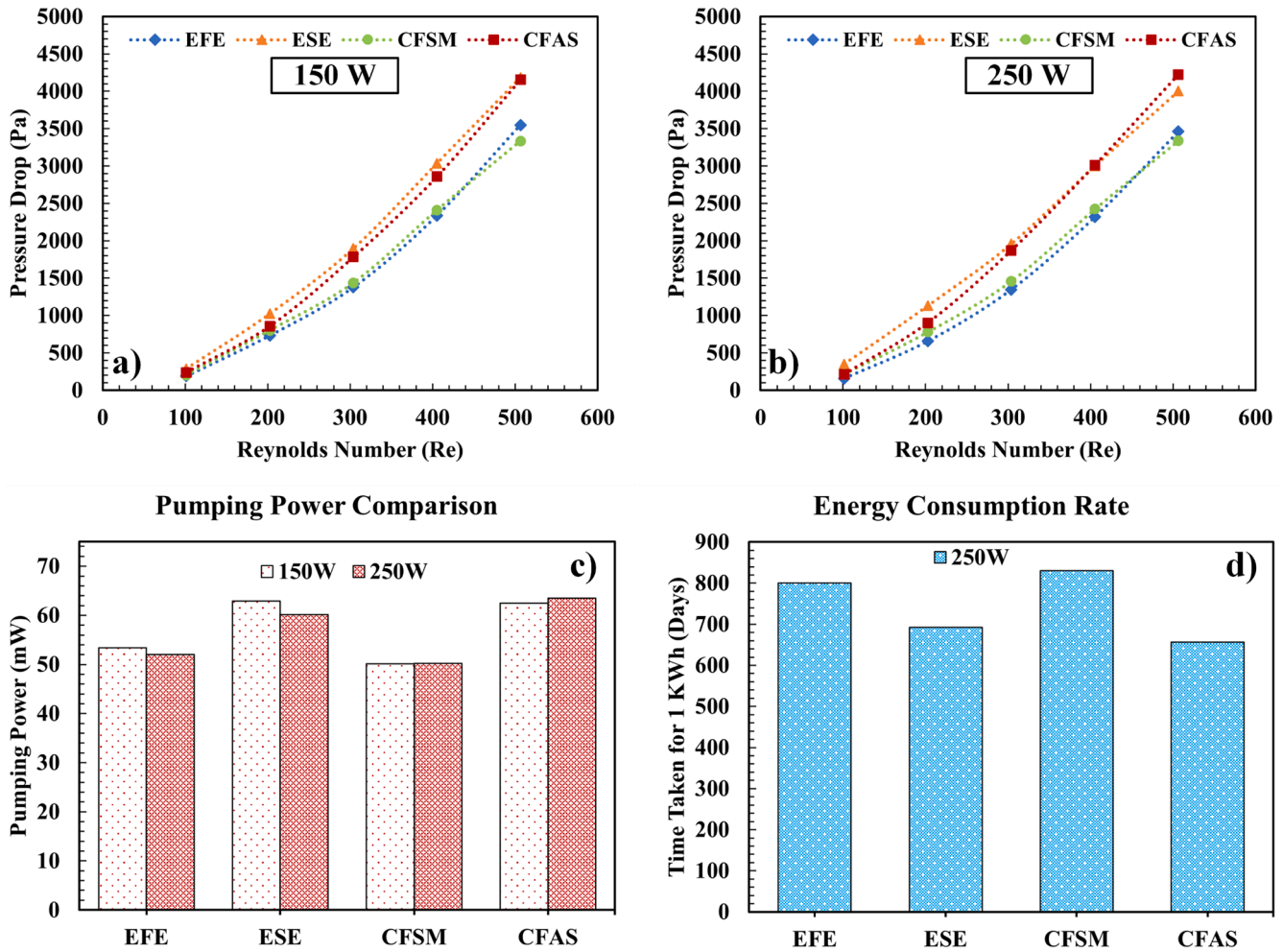


Fig. 10. (a)-(d) Pressure drop and pumping power comparison.

its energy consumption remains still manageable and justifiable due to its thermal performance.

While designs like EFE and CFAS exhibit higher pressure drops, their overall performance justifies these trade-offs. The EFE design offers an effective balance between heat transfer efficiency and energy consumption, making it a cost-effective choice despite its moderate pressure drop. The CFAS design, although it incurs a higher pressure drop and pumping power, provides good thermal performance, and its overall energy consumption remains relatively low as shown in Figs. 10(c) and 10(d). Thus, despite the higher pressure drops, the energy consumption metrics of both EFE and CFAS align well with their heat transfer benefits, making them acceptable choices depending on the specific needs of the application.

#### 5.4. Effect of fin shape on thermohydraulic performance

The thermohydraulic performance of heat sinks is closely tied to the geometric design of the fins, which influences the flow dynamics, heat transfer efficiency, and pressure characteristics of the system. This section discusses how different micro pin-fin heat sink designs—EFE, ESE, CFSM, and CFAS—affect key performance metrics such as the Nusselt number, thermal resistance, and pressure drop, offering insights into the underlying physics that drive these outcomes.

In this study, the EFE design, which features filleted (curved) edges, consistently achieved the highest Nu values across a range of Reynolds numbers ( $Re$ ). The rounded edges in the EFE design likely facilitate smoother fluid flow over the fin surfaces, reducing the formation of

turbulent wake regions that can disrupt the thermal boundary layer. By maintaining a more stable and attached flow, the EFE design enhances convective heat transfer by maximising the effective surface area exposed to the fluid and minimising thermal resistance at the interface.

In contrast, the ESE design, characterised by sharp-edged fins, demonstrated lower Nu values. The sharp edges likely induce early flow separation, creating vortices and turbulent wake regions that, while increasing local heat transfer, disrupt the overall flow pattern and reduce the effective surface area available for heat exchange. The increased turbulence can lead to higher localised heat transfer. It also introduces inefficiencies by causing larger pressure gradients and non-uniform heat transfer distribution, resulting in a less effective overall convective HTC than the EFE design.

The CFSM design, which incorporates secondary flow lanes, exhibited the lowest Nu values among the designs. The secondary lanes led to less direct fluid interaction with the fin surfaces, reducing the overall heat transfer coefficient. These lanes might cause the fluid to bypass certain areas of the fins, leading to lower surface area utilisation and weaker convective heat transfer. The design may also create a more complex flow path, increasing the residence time of the fluid without significantly enhancing heat transfer, resulting in a lower Nu.

The CFAS design, with its innovative astroid splitters, achieved the second-highest Nu values, particularly at lower  $Re$ . The splitters likely act to increase turbulence in a controlled manner, enhancing mixing and ensuring that cooler fluid is continually brought into contact with the hot surfaces. This design likely improves the surface interaction of the fluid, increasing the effective convective heat transfer area and leading

to higher Nu values. However, at higher Re, the increase in turbulence might lead to diminishing returns, as excessive turbulence could disrupt the flow too much, reducing the overall heat transfer efficiency.

Thermal resistance measures a heat sink's ability to dissipate heat, with lower values indicating better performance. The CFAS design consistently exhibited the lowest thermal resistance, particularly at higher Re. The design's astroid splitters likely optimise the flow paths within the heat sink, ensuring a more even distribution of the fluid over the surface area. This enhanced fluid distribution reduces hotspots and maximises the contact between the fluid and the fin surfaces, leading to more efficient heat removal and, consequently, lower thermal resistance. The complex geometry increases the effective surface area without significantly impeding fluid flow, which helps in maintaining low thermal resistance.

In contrast, the CFSM design showed the highest thermal resistance, particularly at lower Re. The design's secondary flow lanes might cause non-uniform flow distribution, leading to areas of stagnant flow where heat builds up. The reduced surface area contacts due to the flow bypassing certain regions result in inefficient heat removal, thereby increasing thermal resistance. Additionally, the potential for flow recirculation within the secondary lanes could further impede heat transfer by trapping hot fluid in certain regions, worsening the thermal resistance.

The EFE and ESE designs exhibited intermediate thermal resistance values, with the EFE generally outperforming the ESE. The filleted edges of the EFE design likely promote smoother fluid flow and better surface contact, reducing thermal resistance compared to the ESE design. The sharper edges in the ESE design may cause flow disruptions that limit the effectiveness of heat removal, leading to higher thermal resistance. These flow disruptions could cause uneven temperature distribution on the fin surfaces, further contributing to increased thermal resistance.

Pressure drop is a critical factor in the design of heat sinks, as it influences the energy required to pump the coolant through the system. The ESE design, with its sharp-edged fins, exhibited one of the highest pressure drops. The sharp edges likely cause significant turbulence and flow separation, which increases the resistance to fluid flow. This increased resistance requires more pumping power to maintain the desired flow rate, leading to higher energy consumption. The substantial pressure gradients created by the sharp edges increase the energy required to overcome these resistances, making the ESE design less energy-efficient in long-term operation.

On the other hand, the CFSM design, featuring secondary flow lanes, demonstrated a moderate pressure drop and the lowest pumping power requirement. The secondary lanes likely help streamline the flow by providing alternate paths, reducing the overall resistance to fluid flow. This design, while not maximising heat transfer, offers better energy efficiency due to the lower pressure drop, which translates to reduced pumping power and lower operational costs. The trade-off here is between reduced heat transfer and improved energy consumption.

The EFE design, with its filleted edges, achieved a balance between pressure drop and thermal performance. The rounded edges minimise flow separation and reduce turbulence, leading to a moderate pressure drop. This design's ability to maintain efficient heat transfer while also reducing the pressure drop makes it a cost-effective option, as it requires less energy for pumping while still providing good thermal performance.

The CFAS design, though resulted in the highest pressure drop, maintained an acceptable energy consumption due to its superior thermal performance. The complex geometry with astroid splitters enhances heat transfer but at the cost of increased flow resistance. The high-pressure drop indicates that the design creates substantial flow disruptions, likely due to the intricate flow paths around the splitters. However, the improved heat transfer efficiency justifies the higher pumping power required, making it suitable for applications where maximising heat dissipation is critical, even at the expense of higher energy use.

Therefore, the shape of the fins plays a crucial role in determining the thermohydraulic performance of micro pin-fin heat sinks. Designs like

EFE, which offers a balance between smooth fluid flow and efficient heat transfer, tend to perform well across all metrics, while more complex designs like CFAS can push the limits of heat transfer at the cost of higher pressure drops. Understanding the interplay between these factors is essential for optimising heat sink design to meet specific thermal management needs.

While a comprehensive comparison including thermal resistance and pumping power is beneficial, it is challenging to produce a direct, like-for-like comparison with conventional heat sinks from the literature due to the varying flow rate, leading to massively different Re and pumping power, and configurations across studies. Additionally, most studies in the literature do not compare thermal resistance across different investigations; instead, they typically compare thermal resistance between designs within the same study. Many comparative studies also do not consistently report values for parameters like pressure drop, further complicating direct comparisons. However, to provide a combine thermohydraulic comparison, we have incorporated a performance improvement factor (Eq. (14)) relying on Nusselt number and pressure drop to provide relevant heat transfer enhancement; to achieve this we have used the experimental values of [15]. The results show that compared to circular pin-fins, the new designs EFE and CFAS, show a combined improvement of 1.30 and 1.33 respectively. Therefore, this further highlights the effectiveness of the mixed geometries in providing a balanced thermohydraulic improvements.

Performance Improvement Factor (PIF):

$$PIF = \frac{\left(\frac{Nu_{(nc)}}{Nu_{(bc)}}\right)}{\left(\frac{\Delta P_{(nc)}}{\Delta P_{(bc)}}\right)^{\frac{1}{3}}} \quad (14)$$

Where nc refers to the new case, and bc is the base case (circular fins) gained from the experimental results of [15].

### 5.5. Building empirical correlation models

The currently available empirical correlation models, including classical models developed by Shah [62] or London or Kosar, et al. [63], are not suitable for the new types of hybrid micro pin fin geometries, even if they initially show good agreement at lower Reynolds numbers. These traditional models, designed for simpler microchannel or pin-fin configurations, fail to account for the complex flow dynamics introduced by the intricate geometries of hybrid micropin setups. While Xu et al.'s correlation, tailored for petaloid geometries, demonstrated reasonable accuracy at lower Reynolds numbers, its applicability diminishes as the flow approaches the transitional regime. In this study, the flow transition occurs between Reynolds numbers 300 and 400, a range where flow behaviour becomes unstable and difficult to model accurately. Xu et al.'s [15] correlation, developed for a broader range of 300 to 1500, reports turbulence around a Reynolds number of 900. However, existing literature suggests that transitional regimes can begin at Reynolds numbers greater than 300 [64]. This transitional behaviour is evident in the graphs of Nusselt number (Nu) and thermal resistance, where the values show only limited increases or massive fluctuations.

Although MSE is a commonly used metric, this research primarily focuses on R<sup>2</sup> and MAPE values due to the different data scales between Rth, Nu, and pressure drops. MAPE values are more generalisable when the data ranges vary significantly in magnitude. Hence, the breakdown of the equations for calculating MSE, MAPE, and R<sup>2</sup> are as follows:

The R<sup>2</sup> (R-squared) is a statistical measure that represents the proportion of the variance in the dependent variable that is predictable from the independent variables given by this equation:

$$R^2 = 1 - \frac{\sum_{i=1}^n (y_i - \hat{y}_i)^2}{\sum_{i=1}^n (y_i - \bar{y})^2} \quad (15)$$

Where:

- $n$  is the number of data points.
- $y_i$  is the real value for  $i^{th}$  data point.
- $\hat{y}_i$  is the prediction for  $i^{th}$  data point.
- $\bar{y}$  is the average of the real values.
- $\sum_{i=1}^n (y_i - \hat{y}_i)^2$  is the sum of squared errors.
- $\sum_{i=1}^n (y_i - \bar{y})^2$  is the total sum of squares (the total variance in the actual values).

The Mean Absolute Percentage Error (MAPE) is a measure of prediction accuracy in a model. The equation calculates the average of the absolute percentage errors between actual and predicted values, expressed as a percentage. The equation for MAPE is:

$$MAPE = \frac{1}{n} \sum_{i=1}^n \left| \frac{y_i - \hat{y}_i}{y_i} \right| \times 100 \tag{16}$$

Where:

- $y_i$  is the real value for  $i^{th}$  data point.
- $\left| \frac{y_i - \hat{y}_i}{y_i} \right|$  is the absolute percentage error for the  $i^{th}$  data point.

The Mean Squared Error (MSE) is used as a quality measure for a model estimator; it calculates the average of the squared differences between actual and predicted values, given by:

$$MSE = \frac{1}{n} \sum_{i=1}^n (y_i - \hat{y}_i)^2 \tag{17}$$

- $(y_i - \hat{y}_i)^2$  is the squared error for the  $i^{th}$  data point.

Despite the limitations of existing correlations, the experimental values from this research remain robust, with the Mean Absolute Percentage Error (MAPE) between Nu, thermal resistance (Rth), and pressure drops ranging between 2.5 % to 7.5 % for power levels of 250 W and 150W. This indicates that the experimental data are consistent and reliable. Notably, the Nusselt number is slightly lower at 250 W compared to 150 W, which can be attributed to the increased thermal load at higher power levels. This higher thermal load may lead to elevated fluid temperatures and reduced heat transfer efficiency due to changes in fluid properties or boundary layer effects under these conditions. Therefore, while existing correlations fall short in predicting the behaviour of hybrid micro pin-fins, the experimental results are robust and give valuable performance insights.

Nonetheless, to develop new correlation models, the data and parameters were combined to assess the Pearson correlation between



Fig. 11. Correlation matrix for parameters.



various dependent and independent variables (DVs and IVs). Fig. 11 shows the correlation matrix, where it is evident that Nu, Re, pressure drop (PD), and power (Pu) have strong positive correlations, while Rth has a strong negative correlation. In many empirical correlation models, Nu is calculated using Reynolds number (Re) and Prandtl number (Pr). The Pr for the flows were calculated depending on the temperature; however, the Pr values vary inconsistently across different models, with only the EFE model showing any significant correlation between Nu and Pr. This inconsistency further highlights the complexity of the dataset and the intricate underlying physics. To determine if Pr significantly influences the dataset, a principal component analysis (PCA) was conducted for feature engineering and to ensure that any power law correlation equations developed are robust and generalisable.

Principal Component Analysis (PCA) is a dimensionality reduction technique used to identify key parameters which influence variability in the original dataset. Although domain knowledge suggested that Nu, PD, Re, and Pr are key variables [63,65], the irregularity and weak correlations of Pr warranted the application of PCA as an additional confirmation. PCA was applied to identify the key variables that contribute most to the variability in the dataset, which is composed of different power configurations and thermal performance metrics. The strategy involved standardising the data to ensure each feature contributed equally to the PCA. PCA was then performed, and the first two principal components were analysed, as they typically capture the most variance in the data. The loadings of the variables were examined to determine which had the most influence on these principal components. Generally, variables with the highest absolute loading values in the first two components are considered the most impactful, providing insight into the underlying structure of the data and allowing for a more focused analysis of the key factors driving the observed patterns.

In this case, Rth and Nu were the most influential. Nevertheless, the other three factors—Re (0.77), PD (0.76), and Pr (0.74)—showed strong and closely matched loading values to Nu (0.80). Therefore, the PCA confirmed the inclusion of Pr as a parameter in forming empirical correlations for the new hybrid micro pin-fins. However, since CFAS and EFE were the two best-performing configurations from the two types of MPFHS setups, power law empirical equations were derived for them, along with their MAPE and R<sup>2</sup> values, to demonstrate the model’s accuracy and variations. Table 3 presents the new empirical correlation equations created using Python and power law equations for the best-performing Cruciform and Exocoetidae-inspired biomorphic heat sinks

5.6. Machine learning-driven analysis

This research employs machine learning algorithms for investigative data analysis and to enhance validation of the dataset; thus, providing an in-depth description of each algorithm goes beyond the scope of this paper. Furthermore, these algorithms have been extensively discussed in the existing literature [10,66–68]. The experimental data results and subsequent empirical correlations yielded high R<sup>2</sup> values. Therefore, a key point of interest was determining whether machine learning algorithms could provide more accurate Nu predictions using Re and Pr and if they can better capture the complex data patterns to show the existence of meaningful relationships and valid patterns in the dataset. As a result, 10 different types of regression models were used.

Firstly, Linear Regression (LR) models the relationship between dependent and independent variables (DV and IV) by fitting a straight

**Table 3**  
Empirical correlations equations.

Design	Equation	Accuracy
EFE	$Nu = 1.9434 \times Re^{0.2126} \times Pr^{0.3517}$	MAPE = 1.34 %; R <sup>2</sup> = 0.987
	$\Delta P = 0.0283 \times Re^{1.8120} \times Pr^{0.2866}$	MAPE = 3.11 %; R <sup>2</sup> = 0.99
CFAS	$Nu = 3.4822 \times Re^{0.1602} \times Pr^{0.1466}$	MAPE = 1.63 %; R <sup>2</sup> = 0.957
	$\Delta P = 0.1737 \times Re^{1.6626} \times Pr^{-0.1492}$	MAPE = 7.06 %; R <sup>2</sup> = 0.98

line. On the other hand, Polynomial Regression (PLR) extends LR by modelling non-linear trends through polynomial relationships. XGBoost (XGB) is an optimised version of a gradient boosting algorithm that enhances prediction accuracy via ensemble learning, and it is highly efficient for structured data. Random Forest (RF) is another ensemble learning method that improves prediction accuracy and robustness by averaging outputs from multiple decision trees. On a different note, Support Vector Regression (SVR) leverages support vector machines to make predictions by finding the optimal hyperplane to minimise errors. K-Nearest Neighbours (KNN) predicts values by averaging the outputs of the closest data points, offering a simple yet effective approach. Ridge Regression (RR) is a regularised version of linear regression that adds a penalty on high coefficients to reduce overfitting; Elastic Net (EN) combines the penalties of Ridge and Lasso regression, balancing variance and bias. MLP Regression, based on a multi-layer perceptron, uses neural networks to model complex, non-linear relationships in data. Lastly, a Combined Model (CM) blends multiple models to enhance prediction accuracy by leveraging their strengths — in this case, it combines MLP, KNN, and LR. The reason multiple different models are compared against each other is to assess and address any overfitting issues. Table 4 shows the initial model performances.

The performance of various predictive models for tNusselt number (Nu) based on Reynolds number (Re) and Prandtl number (Pr) revealed significant differences in accuracy and reliability. They were categorised into four different categories discussed in the following paragraphs.

Very High Accuracy Models, Possible Overfitting (R<sup>2</sup> > 0.95), include XGBoost, Polynomial Regression, and Random Forest. XGBoost stands out with a perfect R<sup>2</sup> of 1.00, therefore there is overfitting. However, its near-zero MSE and MAPE indicate that it effectively minimises prediction errors and handles the non-linearity and interactions between Re and Pr adeptly, and, thus, is too reliant on this dataset. Polynomial Regression also performs exceedingly well with an R<sup>2</sup> of 0.9950, leveraging polynomial terms to capture intricate relationships between the variables. This model’s high performance is due to its flexibility in fitting complex patterns, despite a slight increase in error metrics compared to XGBoost. Random Forest achieves an R<sup>2</sup> of 0.9748, demonstrating strong predictive power with an ensemble of decision trees that reduces overfitting and captures a broad range of interactions between Re and Pr. The slightly higher MSE and MAPE compared to XGBoost and Polynomial Regression suggest it might not model the data’s most intricate patterns as precisely.

High Accuracy Models (0.95 > R<sup>2</sup> > 0.80) consist of Support Vector Regression (SVR). SVR, with an R<sup>2</sup> of 0.8940, shows effective performance but with higher MSE and MAPE, which might be due to its sensitivity to the choice of kernel and hyperparameters. Although SVR handles non-linearities well, its performance is slightly less robust than very high-accuracy models. KNN, with an R<sup>2</sup> of 0.8026, offers reasonable predictions but struggles with higher MSE and MAPE due to its reliance on local data and potential sensitivity to the choice of k-neighbors.

Good Accuracy Models (0.80 > R<sup>2</sup> > 0.70) included Linear Regression and Ridge Regression, with R<sup>2</sup> values of 0.7833 and 0.7808 respectively, show basic predictive capabilities but are limited by their

**Table 4**  
Different regression algorithm performance.

Model	MSE	MAPE	R <sup>2</sup>
XGBoost	0.000	0.07 %	1
Polynomial Regression	0.010	0.72 %	0.995
Random Forest	0.050	1.67 %	0.9748
Support Vector Regression	0.209	3.17 %	0.894
K-Nearest Neighbors	0.099	2.72 %	0.8026
Linear Regression	0.108	2.95 %	0.7833
Ridge Regression	0.110	2.79 %	0.7808
Combined Model	0.134	2.26 %	0.7317
Elastic Net	0.262	3.30 %	0.4762
MLP Regression	0.388	5.21 %	0.2225

assumptions of linear relationships. Ridge Regression improves upon Linear Regression by adding regularisation to handle multicollinearity. Yet, both models fail to capture the non-linear interactions as effectively as more advanced techniques, resulting in higher errors. The combined model produces even lower accuracies than a single model.

Low Accuracy Models ( $R^2 < 0.70$ ) are represented by Elastic Net and MLP Regression. Elastic Net, with  $R^2$  of 0.4762, demonstrates poor performance due to the challenges of balancing L1 and L2 regularization, which may not suit the complex relationships in the dataset. The high MSE and MAPE suggest that the regularisation terms are not effectively tuning the model. MLP Regression also exhibits the lowest  $R^2$  of 0.2225, attributed to its complexity potential underfitting issues and limited data. The model’s architecture might not be well-suited for this problem, leading to significant inaccuracies in prediction.

Overall, XGBoost and Polynomial Regression are the most reliable models for predicting Nu, offering the highest accuracy and lowest errors due to their ability to handle non-linearity and complex interactions. Nevertheless, these show signs of overfitting too. Models in the high accuracy category are effective but may not provide the same level of precision due to their inherent limitations. The lower accuracy models show notable deficiencies in capturing the data’s nuances, indicating a need for different modelling approaches or further optimisation to improve performance. Therefore to cross-validate the results and alleviate overfitting issues for better data generalisation. The original dataset was synthetically augmented with large Gaussian noise to distort the dataset and further analyse if the models can still make robust predictions. The reason Gaussian noise was used for regularisation over other methods is due to its versatility and continuity in handling data. Additionally, gaussian methods have previously yielded good performance results [52]. As in the original code, *Re* and *Pr* data were standardised using ‘StandardScaler’ so the features have mean 0 and standard deviation 1 after scaling, a noise of scale of 0.5 of standard deviation is added which is quite significant. The specific equation for generating Gaussian noise would be:

$$\text{Noise} = \sigma \cdot Z \tag{18}$$

Where:

- Z is a random variable sampled from the standard normal distribution  $N(0,1)$
- $\sigma = 0.5$  is the standard deviation.

So, for each data point  $y_i$ , the noisy version would be:

$$\text{Noisy } y_i = y_i + \sigma \cdot Z_i$$

Where:  $Z_i$  is sampled from  $N(0,1)$  independently for each data point.

Gaussian noise was chosen for its effectiveness in replicating minor variations commonly observed in experimental measurements, helping to prevent overfitting by introducing controlled random variability. Compared to standard scaling, which uniformly adjusts data, Gaussian noise allows for more realistic, small-scale fluctuations that align with natural measurement uncertainties, thereby better simulating the variability in experimental conditions. By simulating realistic measurement uncertainties, Gaussian noise enhances the model’s robustness, making it less sensitive to minor discrepancies and improving predictive accuracy across diverse conditions in the dataset.

The addition of Gaussian noise had an interesting impact on the performance of various regression models used to predict Nu based on *Re* and *Pr*. Fig. 12 shows the comparison between the original and augmented datasets. Initially, the models trained on the original dataset demonstrated near-perfect performance metrics, with XGBoost achieving an MSE of 0.0001, a MAPE of 0.07 %, and an  $R^2$  of 1. These metrics, while impressive, suggest a potential risk of overfitting, where the model might be capturing noise and specificities of the training data rather than generalisable patterns. Hence, introducing substantial noise allowed assessment of the model’s ability to generalise beyond the overly specific patterns of the original data. The augmentation showed that models could better handle data variability, leading to improvements.

Nonetheless, such perfect predictions shown by XGB are perhaps unrealistic in a real-world scenario, therefore further assessment of XGB is required. Random Forest’s performance improved from an MSE of 0.0498, a MAPE of 1.67 %, and an  $R^2$  of 0.9748 to an MSE of 0.0096, a MAPE of 0.76 %, and an  $R^2$  of 0.9951. Similarly, SVR’s metrics improved from an MSE of 0.2093 to 0.0973, with MAPE decreasing from 3.17 % to 2.02 %, and  $R^2$  increasing from 0.8940 to 0.9507. The KNN and Polynomial Regression models also exhibited enhanced performance, reflecting a robust generalisation ability after augmentation. Therefore, based on the overall performance of  $R^2$  and MAPE and considering potential overfitting issues, PLR and RF are perhaps the most suitable models for future predictions of Nu.

These results underscore the utility of data augmentation in capturing complex relationships. The substantial noise introduced in the augmentation process helped simulate real-world variability, making

## Model Performance

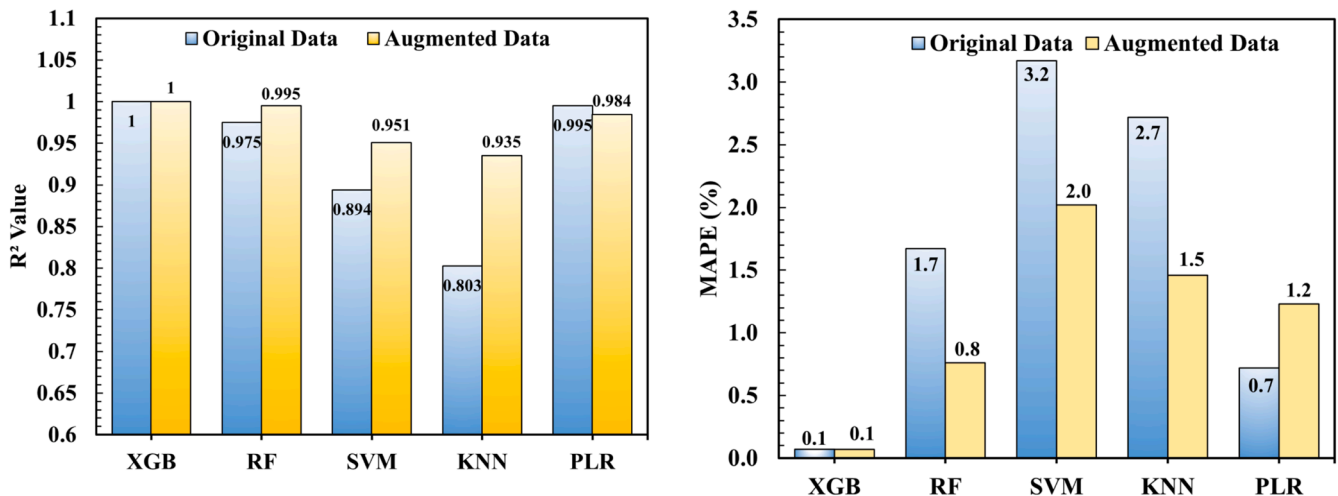


Fig. 12. Model comparison for original and augmented synthetic data.

the models more adept at handling noise and less prone to overfitting. This process is particularly valuable for predicting  $Nu$  from  $Re$  and  $Pr$ , as it helps in modelling the intricate and often non-linear relationships between these variables. Moreover, using augmented data is beneficial in the context of empirical correlation models, where complex relationships might be oversimplified. Traditional empirical models often rely on limited data or simplistic correlations, which may not capture the true dynamics of the system. By contrast, regression models trained with augmented data can explore a broader range of relationships and interactions, providing more accurate and reliable predictions.

The overall data analysis revealed that XGBoost and Polynomial Regression consistently outperform other models, with the highest  $R^2$  values and lowest MAPE. These models excel due to their ability to capture complex non-linear relationships in the data—XGBoost through its ensemble tree-based structure, which reduces variance and improves generalisation, and Polynomial Regression through its flexibility in fitting curved relationships in the dataset. Data augmentation further enhances their performance, as seen in Fig. 11, by providing a more diverse dataset that strengthens model robustness and reduces error rates.

In contrast, models like K-Nearest Neighbours (KNN) and Support Vector Regression (SVR) perform comparatively worse, with lower  $R^2$  values. KNN struggles with complex datasets because it relies heavily on local data points, which can lead to overfitting in certain areas and underperformance in others. SVR, while effective for some regression tasks, has difficulty capturing non-linear patterns without significant tuning, which may explain its lower accuracy here. Linear models, such as Linear Regression and Elastic Net, perform the worst due to their limitations in capturing non-linear relationships, which can be the case in thermohydraulic datasets. This comparative discussion highlights each model's strengths and limitations, providing insights into why certain approaches are more effective for complex predictive tasks like this one.

It is important to acknowledge that the dataset used is limited, and acquiring more experimental data is both expensive and impractical. Thus, data augmentation becomes a crucial technique to enhance the robustness and accuracy of the models without the need for extensive new data collection. This approach supports agile manufacturing concepts by offering a time-efficient method to improve model performance and adaptability. Therefore, the augmentation of data with a large Gaussian noise scale has proven to be a powerful technique in improving model performance, capturing complex relationships, and aligning with agile manufacturing principles. The enhanced generalisation, reflected in improved MAPE and  $R^2$  values, demonstrates the practical benefits of this approach in handling real-world data variability and refining predictions. However, this data-driven approach for exploration is aligned with the ethos of continuous improvement via technology in advancing manufacturing efficiency [69] and provides a good baseline for future predictions of thermohydraulic performance without using extensive datasets.

## 6. Conclusion

In summary, this research illustrates the effectiveness and limitations of various innovative micro pin-fin configurations in assessing the thermohydraulic performance of biomorphic heat sinks. By integrating different design strategies, agile manufacturing, experimental methods, and machine learning approaches, the study offers a novel perspective on the design and production of hybrid biomorphic pin-fins, potentially reducing production time, development costs, and manufacturing expenses. The key conclusions were:

- The Exocoetidae-inspired pin-fins with filleted edges (EFE) and Cruciform-inspired pin-fins with a novel type of astroid splitters (CFAS) outperformed other designs in terms of Nusselt Number ( $Nu$ ), thermal resistance, and pressure drops. These new designs achieve a

23 % to 45 % enhancement in heat transfer at lower Reynolds numbers compared to existing designs in the literature, with manageable increases in pumping power and energy consumption.

- Further thermal assessments reveal that adding secondary lanes or sharp-edged features results in uneven heat distributions, leading to increased turbulence and less efficient heat transfer. However, secondary lanes do help reduce system pressure drop.
- New empirical correlations and machine learning predictions demonstrate high accuracy in forecasting Nusselt Numbers, streamlining design optimisation and providing rapid performance assessments. Among the tested models, ensemble methods such as XGBoost, Random Forest, and Polynomial Regression produced the most accurate results, with a mean absolute percentage error of less than 3 % and high  $R^2$  values.

Overall, this study enhances our understanding of pin-fin heat sink designs by highlighting the advantages of unconventional designs and the benefits of integrating diverse approaches. Combining advanced design techniques with machine learning can significantly improve pin-fin performance, reduce size, cost, and development time, and enhance energy efficiency in next-generation heat sink solutions. Future research should focus on optimising the distribution of pin-fin segments and developing more robust methods for using limited datasets to provide more accurate predictions of thermohydraulic parameters.

## CRedit authorship contribution statement

**Mohammad Harris:** Writing – review & editing, Writing – original draft, Visualization, Validation, Project administration, Methodology, Investigation, Formal analysis, Data curation, Conceptualization. **Hamza Babar:** Writing – review & editing, Visualization, Validation, Methodology, Investigation, Formal analysis, Data curation. **Hongwei Wu:** Writing – review & editing, Supervision, Resources, Project administration, Funding acquisition, Formal analysis, Conceptualization.

## Declaration of competing interest

The authors declare that they have no known competing financial interests or personal relationships that could have appeared to influence the work reported in this paper.

## Acknowledgement

The authors would like to acknowledge the financial support from the Engineering and Physical Science Research Council (EPSRC), UK (Grant No. EP/X038319/1). This support was provided within the framework of the Horizon Europe project Marie Skłodowska-Curie Actions (MSCA), with Grant No. 101082394. Artificial intelligence-related tools have been used for checking grammar and readability purposes.

## Data availability

Data will be made available on request.

## References

- [1] Z. He, Y. Yan, Z. Zhang, Thermal management and temperature uniformity enhancement of electronic devices by micro heat sinks: a review, *Energy* 216 (2021) 119223, <https://doi.org/10.1016/j.energy.2020.119223>.
- [2] B. Chang, T. Yuan, Y. Wang, H. Guo, Z. Li, L. Zhao, C. Zhang, S. Peng, J. Deng, Cooling performance enhancement of electric vehicle film capacitor for ultra-high temperatures using micro-channel cold plates thermal management system, *Int. J. Heat Mass Transf.* 233 (2024) 126037, <https://doi.org/10.1016/j.ijheatmasstransfer.2024.126037>.
- [3] J. Ning, X. Wang, H. Huang, S. Wang, W. Yan, Topology optimized novel additively manufactured heat sink: experiments and numerical simulations, *Energy Convers. Manage* 286 (2023) 117024, <https://doi.org/10.1016/j.enconman.2023.117024>.

- [4] G. Chen, X. Jiang, Y. Li, J. Bai, S.W. Ali Shah, Y. Gao, Y. Tang, S. Zhang, C. Pan, A highly efficient and sustainable heat sink via liquid film boiling in hybrid mesh with active liquid supply, *Energy Convers. Manage* 277 (2023) 116688, <https://doi.org/10.1016/j.enconman.2023.116688>.
- [5] M. Harris, H. Wu, W. Zhang, A. Angelopoulou, Overview of recent trends in microchannels for heat transfer and thermal management applications, *Chemical Engineering and Proc. Process Int.* 181 (2022) 109155, <https://doi.org/10.1016/j.cep.2022.109155>.
- [6] N. Van Toan, K. Ito, T.T.K. Tuoi, M. Toda, P.-H. Chen, M.F.M. Sabri, J. Li, T. Ono, Micro-heat sink based on silicon nanowires formed by metal-assisted chemical etching for heat dissipation enhancement to improve performance of micro-thermoelectric generator, *Energy Convers. Manage* 267 (2022) 115923, <https://doi.org/10.1016/j.enconman.2022.115923>.
- [7] J. Lin, X. Liu, S. Li, C. Zhang, S. Yang, A review on recent progress, challenges and perspective of battery thermal management system, *Int. J. Heat Mass Transf.* 167 (2021) 120834, <https://doi.org/10.1016/j.ijheatmasstransfer.2020.120834>.
- [8] P. Bhandari, K.S. Rawat, Y.K. Prajapati, D. Padalia, L. Ranakoti, T. Singh, Design modifications in micro pin fin configuration of microchannel heat sink for single phase liquid flow: a review, *J. Energy Storage* 66 (2023) 107548, <https://doi.org/10.1016/j.est.2023.107548>.
- [9] B. Yu, Z. Lu, B. Wang, X. Wang, J. Lou, L. Yang, W. Li, A bioinspired programmable Self-Organization approach for designing additively manufactured heat sinks, *Energy Convers. Manage* 286 (2023) 116996, <https://doi.org/10.1016/j.enconman.2023.116996>.
- [10] M. Harris, H. Wu, A. Angelopoulou, W. Zhang, Z. Hu, Y. Xie, Heat transfer optimisation using novel biomorphic pin-fin heat sinks: an integrated approach via design for manufacturing, numerical simulation, and machine learning, *Thermal Sci. Eng. Progress* 51 (2024) 102606, <https://doi.org/10.1016/j.tsep.2024.102606>.
- [11] H.E. Ahmed, B.H. Salman, A.Sh. Kherbeet, M.I. Ahmed, Optimization of thermal design of heat sinks: a review, *Int. J. Heat Mass Transf.* 118 (2018) 129–153, <https://doi.org/10.1016/j.ijheatmasstransfer.2017.10.099>.
- [12] Y. Peles, A. Koşar, C. Mishra, C.-J. Kuo, B. Schneider, Forced convective heat transfer across a pin fin micro heat sink, *Int. J. Heat Mass Transf.* 48 (2005) 3615–3627, <https://doi.org/10.1016/j.ijheatmasstransfer.2005.03.017>.
- [13] A. Siu-Ho, W. Qu, F. Pfefferkorn, Experimental Study of Pressure Drop and Heat Transfer in a Single-Phase Micropin-Fin Heat Sink, *J. Electron. Packag.* 129 (2007) 479–487, <https://doi.org/10.1115/1.2804099>.
- [14] A. Shemelash, B. Tamrat, M. Temesgen, R. Gopal, B. Desalegn, H. Mulugeta, H.G. Solomon, Multi-objective optimization of a Fibonacci phyllotaxis micro pin-fin heat sink, *Heat Transfer n/a* (2024). <https://doi.org/10.1002/htj.23083>.
- [15] Y. Xu, L. Li, J. Wang, Experimental and numerical investigations of the thermal-hydraulic characteristics of novel micropin-fin heat sinks, *Int. J. Heat Mass Transf.* 209 (2023) 124079, <https://doi.org/10.1016/j.ijheatmasstransfer.2023.124079>.
- [16] A.R. Roozbehi, M. Zabetian Targhi, M.M. Heyhat, A. Khatibi, Modified hexagonal pin fins for enhanced thermal-hydraulic performance of micro-pin fin heat sinks, *Int. J. Numer. Methods Heat. Fluid. Flow.* 33 (2023) 2902–2926, <https://doi.org/10.1108/HFF-02-2023-0053>.
- [17] M.O. Qidwai, I.A. Badruddin, S. Kamangar, N.Z. Khan, M.A. Khan, M.N. Khan, Heat transfer enhancement in multijet micropin fin heat sink, *Numer. Heat Transf. Part A: Appl.* 0 (2023) 1–20. <https://doi.org/10.1080/10407782.2023.2294349>.
- [18] D. Gupta, P. Saha, S. Roy, Multi-Objective Optimization of the Perforated Micro Pin-Fin Heat Sink Using Non-Dominated Sorting Genetic Algorithm-II Coupled With Computational Fluid Dynamics Simulation, *J. Heat Transfer* 144 (2022), <https://doi.org/10.1115/1.4054761>.
- [19] M. Harris, H. Wu, J. Sun, Investigating Heat Transfer and Flow Characteristics under Different Wall Heating Conditions in Novel Micro Pin-Fin Heat Sinks, in: 9th World Congress on Momentum, Heat and Mass Transfer (MHMT 2024), Avestia, London, 2024, <https://doi.org/10.11159/enfht24.328>.
- [20] H. Xie, B. Yang, S. Zhang, M. Song, Research on the mechanism of heat transfer enhancement in microchannel heat sinks with micropin fins, *Int. J. Energy Res.* 44 (2020) 3049–3065, <https://doi.org/10.1002/er.5135>.
- [21] Y. Xu, L. Li, Z. Yan, Experimental investigations of the flow boiling characteristics of green refrigerants in a novel petaloid micropin-fin heat sink, *Int. J. Heat Mass Transf.* 212 (2023) 124243, <https://doi.org/10.1016/j.ijheatmasstransfer.2023.124243>.
- [22] T. David, D. Mandler, A. Mosyak, A. Bar-Cohen, G. Hetsroni, Thermal Management of Time-Varying High Heat Flux Electronic Devices, *J. Electron. Packag.* 136 (2014), <https://doi.org/10.1115/1.4027325>.
- [23] T. Ambreen, A. Saleem, C.W. Park, Pin-fin shape-dependent heat transfer and fluid flow characteristics of water- and nanofluid-cooled micropin-fin heat sinks: square, circular and triangular fin cross-sections, *Appl. Therm. Eng.* 158 (2019) 113781, <https://doi.org/10.1016/j.applthermaleng.2019.113781>.
- [24] T. Ambreen, A. Saleem, C.W. Park, Numerical analysis of the heat transfer and fluid flow characteristics of a nanofluid-cooled micropin-fin heat sink using the Eulerian-Lagrangian approach, *Powder Technol.* 345 (2019) 509–520, <https://doi.org/10.1016/j.powtec.2019.01.042>.
- [25] F. Keshavarz, A. Mirabdollah Lavasani, H. Bayat, Numerical analysis of effect of nanofluid and fin distribution density on thermal and hydraulic performance of a heat sink with drop-shaped micropin fins, *J. Therm. Anal. Calorim.* 135 (2019) 1211–1228, <https://doi.org/10.1007/s10973-018-7711-z>.
- [26] B. Markal, A. Evcimen, O. Aydin, Effect of inlet temperature on flow boiling behavior of expanding micro-pin-fin type heat sinks, *Int. Commun. Heat Mass Transfer* 149 (2023) 107143, <https://doi.org/10.1016/j.icheatmasstransfer.2023.107143>.
- [27] B. Markal, A. Evcimen, Transient behavior of flow boiling in structured microchannels under sudden and highly variable heat loads, *Int. Commun. Heat Mass Transfer* 154 (2024) 107431, <https://doi.org/10.1016/j.icheatmasstransfer.2024.107431>.
- [28] S.K. Rajan, A. Kaul, T.E. Sarvey, G.S. May, M.S. Bakir, Monolithic Microfluidic Cooling of a Heterogeneous 2.5-D FPGA With Low-Profile 3-D Printed Manifolds, *IEEE Trans. Comp. Pack. Manuf. Technol.* 11 (2021) 974–982, <https://doi.org/10.1109/TCPMT.2021.3082013>.
- [29] T.E. Sarvey, Y. Zhang, C. Cheung, R. Gutala, A. Rahman, A. Dasu, M.S. Bakir, Monolithic Integration of a Micropin-Fin Heat Sink in a 28-nm FPGA, *IEEE Trans. Comp. Pack. Manuf. Technol.* 7 (2017) 1617–1624, <https://doi.org/10.1109/TCPMT.2017.2740721>.
- [30] X. Zhang, X. Han, T.E. Sarvey, C.E. Green, P.A. Kottke, A.G. Fedorov, Y. Joshi, M. S. Bakir, Three-Dimensional Integrated Circuit With Embedded Microfluidic Cooling: technology, Thermal Performance, and Electrical Implications, *J. Electron. Packag.* 138 (2016), <https://doi.org/10.1115/1.4032496>.
- [31] A. Renfer, M.K. Tiwari, R. Tiwari, F. Alfieri, T. Brunschweiler, B. Michel, D. Poulikakos, Microvortex-enhanced heat transfer in 3D-integrated liquid cooling of electronic chip stacks, *Int. J. Heat Mass Transf.* 65 (2013) 33–43, <https://doi.org/10.1016/j.ijheatmasstransfer.2013.05.066>.
- [32] Q. Shi, Q. Liu, X. Yao, C. Sun, X. Ju, M.M. Abd El-Samie, C. Xu, Optimal design on irregular polygon topology for the manifold micro-pin-fin heat sink, *Int. Commun. Heat Mass Transfer* 141 (2023) 106574, <https://doi.org/10.1016/j.icheatmasstransfer.2022.106574>.
- [33] X. Han, A. Fedorov, Y. Joshi, Flow Boiling in Microgaps for Thermal Management of High Heat Flux Microsystems, *J. Electron. Packag.* 138 (2016), <https://doi.org/10.1115/1.4034317>.
- [34] Y. Zhang, A. Dembla, M.S. Bakir, Silicon Micropin-Fin Heat Sink With Integrated TSVs for 3-D ICs: tradeoff Analysis and Experimental Testing, *IEEE Trans. Components, Pack. Manuf. Technol.* 3 (2013) 1842–1850, <https://doi.org/10.1109/TCPMT.2013.2267492>.
- [35] T.E. Sarvey, Y. Hu, C.E. Green, P.A. Kottke, D.C. Woodrum, Y.K. Joshi, A. G. Fedorov, S.K. Sitarman, M.S. Bakir, Integrated Circuit Cooling Using Heterogeneous Micropin-Fin Arrays for Nonuniform Power Maps, *IEEE Trans. Components Pack. Manuf. Technol.* 7 (2017) 1465–1475, <https://doi.org/10.1109/TCPMT.2017.2704525>.
- [36] Y. Oh, Z. Guo, Prediction of Nusselt number in microscale pin fin heat sinks using artificial neural networks, *HTR* 54 (2023), <https://doi.org/10.1615/HeatTransRes.2022044987>.
- [37] H. Ehsani, F.N. Roudbari, S.S. Namaghi, p. Jalili, D.D. Ganji, Investigating thermal performance enhancement in perforated pin fin arrays for cooling electronic systems through integrated CFD and deep learning analysis, *Results. Eng.* 22 (2024) 102016, <https://doi.org/10.1016/j.rineng.2024.102016>.
- [38] V. Çorumlu, V. Altıntaş, M. Abuşka, Evaluation of prediction and modeling performance using machine learning methods for thermal parameters of heat sinks under forced convection: the case of external validation, *Int. Commun. Heat Mass Transfer* 151 (2024) 107228, <https://doi.org/10.1016/j.icheatmasstransfer.2023.107228>.
- [39] N. Fallatafti, S. Rangarajan, Y. Hadad, C. Arvin, K. Sikka, C.H. Hoang, G. Mohsenian, V. Radmard, S. Schiffres, B. Sammakia, Shape optimization of hotspot targeted micro pin fins for heterogeneous integration applications, *Int. J. Heat Mass Transf.* 192 (2022) 122897, <https://doi.org/10.1016/j.ijheatmasstransfer.2022.122897>.
- [40] N.P. Nguyen, E. Maghsoudi, S.N. Roberts, B. Kwon, Shape optimization of pin fin array in a cooling channel using genetic algorithm and machine learning, *Int. J. Heat Mass Transf.* 202 (2023) 123769, <https://doi.org/10.1016/j.ijheatmasstransfer.2022.123769>.
- [41] M. Tabatabaei Malazi, K. Kaya, A.B. Çolak, A.S. Dalkılıç, CFD and ANN analyses for the evaluation of the heat transfer characteristics of a rectangular microchannel heat sink with various cylindrical pin-fins, *Heat Mass Transfer* (2024), <https://doi.org/10.1007/s00231-024-03496-7>.
- [42] K. Nilpueng, P. Kaseethong, M. Mesgarpour, M.S. Shadloo, S. Wongwises, A novel temperature prediction method without using energy equation based on physics-informed neural network (PINN): a case study on plate- circular/square pin-fin heat sinks, *Eng. Anal. Bound. Elem.* 145 (2022) 404–417, <https://doi.org/10.1016/j.enganabound.2022.09.032>.
- [43] S. Ghosh, S. Mondal, J.S. Kapat, A. Ray, Parametric shape optimization of pin fin arrays using a multi-fidelity surrogate model based Bayesian method, *Appl. Therm. Eng.* 247 (2024) 122876, <https://doi.org/10.1016/j.applthermaleng.2024.122876>.
- [44] B. Heidarsheh, A. Abidi, S.M. Sajadi, Y. Yuan, A.S. El-Shafay, H.Ş. Aybar, Numerical study and optimization of thermal efficiency for a pin fin heatsink with nanofluid flow by modifying heatsink geometry, *Case Stud. Thermal Eng.* 55 (2024) 104125, <https://doi.org/10.1016/j.csite.2024.104125>.
- [45] S.S. Pai, J.A. Weibel, Machine-learning-aided design optimization of internal flow channel cross-sections, *Int. J. Heat Mass Transf.* 195 (2022) 123118, <https://doi.org/10.1016/j.ijheatmasstransfer.2022.123118>.
- [46] A. Tikadar, S. Kumar, Machine learning approach to predict heat transfer and fluid flow characteristics of integrated pin fin-metal foam heat sink, *Numer. Heat Transf. Part B Fund.* 0 (n.d.) 1–26. <https://doi.org/10.1080/10407790.2023.2266772>.
- [47] B. Markal, Y.E. Karabacak, A. Evcimen, Machine-learning-based modeling of saturated flow boiling in pin-fin micro heat sinks with expanding flow passages, *Int. Commun. Heat Mass Transfer* 158 (2024) 107870, <https://doi.org/10.1016/j.icheatmasstransfer.2024.107870>.

- [48] H. Lee, G. Lee, K. Kim, D. Kong, H. Lee, Multimodal machine learning for predicting heat transfer characteristics in micro-pin fin heat sinks, *Case Stud. Thermal Eng.* 57 (2024) 104331, <https://doi.org/10.1016/j.csite.2024.104331>.
- [49] G. Zhu, S. Liu, D. Zhang, W. Chen, J. Li, T. Wen, Transfer learning model to predict flow boiling heat transfer coefficient in mini channels with micro pin fins, *Int. J. Heat Mass Transf.* 220 (2024) 125020, <https://doi.org/10.1016/j.ijheatmasstransfer.2023.125020>.
- [50] K. Kim, H. Lee, M. Kang, G. Lee, K. Jung, C.R. Kharangate, M. Ashoghi, K. E. Goodson, H. Lee, A machine learning approach for predicting heat transfer characteristics in micro-pin fin heat sinks, *Int. J. Heat Mass Transf.* 194 (2022) 123087, <https://doi.org/10.1016/j.ijheatmasstransfer.2022.123087>.
- [51] M. Harris, H. Wu, Numerical Simulation of Heat Transfer Performance in Novel Biomimetic Pin-Fin Heat Sinks, in: *Avestia, Lisbon*, 2023. <https://doi.org/10.1111/59/enfht23.166>.
- [52] M. Harris, A. Angelopoulou, H. Wu, W. Zhang, Comparative Analysis of Micro/Minichannel Flow Boiling Pattern Recognition and Classification using Clustering Algorithms, in: *IEEE 14th International Conference on Pattern Recognition Systems, Institute of Electrical and Electronics Engineers (IEEE)*, 2024. <https://researchprofiles.herts.ac.uk/en/publications/comparative-analysis-of-micromini-channel-flow-boiling-pattern-rec>. accessed August 14, 2024.
- [53] H. Babar, H. Wu, W. Zhang, Investigating the performance of conventional and hydrophobic surface heat sink in managing thermal challenges of high heat generating components, *Int. J. Heat Mass Transf.* 216 (2023) 124604, <https://doi.org/10.1016/j.ijheatmasstransfer.2023.124604>.
- [54] H. Babar, H. Wu, H.M. Ali, W. Zhang, Hydrothermal performance of inline and staggered arrangements of airfoil shaped pin-fin heat sinks: a comparative study, *Thermal Sci. Eng. Progress* 37 (2023) 101616, <https://doi.org/10.1016/j.tsep.2022.101616>.
- [55] A. Gunasekaran, Y.Y. Yusuf, E.O. Adeleye, T. Papadopoulos, D. Kovvuri, D.G. Geyi, Agile manufacturing: an evolutionary review of practices, *Int. J. Prod. Res.* 57 (2019) 5154–5174, <https://doi.org/10.1080/00207543.2018.1530478>.
- [56] P. Zhang, T. Cui, Q. Li, Effect of surface roughness on thermal contact resistance of aluminium alloy, *Appl. Therm. Eng.* 121 (2017) 992–998, <https://doi.org/10.1016/j.applthermaleng.2017.04.142>.
- [57] H.M. Ali, W. Arshad, Thermal performance investigation of staggered and inline pin fin heat sinks using water based rutile and anatase TiO<sub>2</sub> nanofluids, *Energy Convers. Manage.* 106 (2015) 793–803, <https://doi.org/10.1016/j.enconman.2015.10.015>.
- [58] E.M.S. El-Said, G.B. Abdelaziz, S.W. Sharshir, A.H. Elsheikh, A.M. Elsaid, Experimental investigation of the twist angle effects on thermo-hydraulic performance of a square and hexagonal pin fin array in forced convection, *Int. Commun. Heat Mass Transfer* 126 (2021) 105374, <https://doi.org/10.1016/j.icheatmasstransfer.2021.105374>.
- [59] T. Ambreen, M.-H. Kim, Effect of fin shape on the thermal performance of nanofluid-cooled micro pin-fin heat sinks, *Int. J. Heat Mass Transf.* 126 (2018) 245–256, <https://doi.org/10.1016/j.ijheatmasstransfer.2018.05.164>.
- [60] L. Chai, G. Xia, M. Zhou, J. Li, J. Qi, Optimum thermal design of interrupted microchannel heat sink with rectangular ribs in the transverse microchambers, *Appl. Therm. Eng.* 51 (2013) 880–889, <https://doi.org/10.1016/j.applthermaleng.2012.10.037>.
- [61] M.W. Uddin, N.S. Sifat, Comparative study on hydraulic and thermal characteristics of minichannel heat sink with different secondary channels in parallel and counter flow directions, *Int. J. Thermofl.* 17 (2023) 100296, <https://doi.org/10.1016/j.ijft.2023.100296>.
- [62] R.K. Shah, Thermal entry length solutions for the circular tube and parallel plates, in: *Proceedings of 3rd National Heat and Mass Transfer Conference, Indian Institute of Technology Bombay, Delhi*, 1975, pp. 11–75.
- [63] A. Kosar, C.-J. Kuo, Y. Peles, Hydrooil-Based Micro Pin Fin Heat Sink, *Am. Soc. Mech. Eng. Digital Collect.* (2007) 563–570, <https://doi.org/10.1115/IMECE2006-13257>.
- [64] D. Li, *Encyclopedia of Microfluidics and Nanofluidics*, Springer Science & Business Media, 2008.
- [65] M. Liu, D. Liu, S. Xu, Y. Chen, Experimental study on liquid flow and heat transfer in micro square pin fin heat sink, *Int. J. Heat Mass Transf.* 54 (2011) 5602–5611, <https://doi.org/10.1016/j.ijheatmasstransfer.2011.07.013>.
- [66] J. Mohammadpour, S. Husain, F. Salehi, A. Lee, Machine learning regression-CFD models for the nanofluid heat transfer of a microchannel heat sink with double synthetic jets, *Int. Commun. Heat Mass Transfer* 130 (2022) 105808, <https://doi.org/10.1016/j.icheatmasstransfer.2021.105808>.
- [67] D.N. Cosenza, L. Korhonen, M. Maltamo, P. Packalen, J.L. Strunk, E. Næsset, T. Gobakken, P. Soares, M. Tomé, Comparison of linear regression, k-nearest neighbour and random forest methods in airborne laser-scanning-based prediction of growing stock, *For. Int. J. Forest Res. h* 94 (2021) 311–323, <https://doi.org/10.1093/forestry/cpaa034>.
- [68] J. Cai, K. Xu, Y. Zhu, F. Hu, L. Li, Prediction and analysis of net ecosystem carbon exchange based on gradient boosting regression and random forest, *Appl. Energy* 262 (2020) 114566, <https://doi.org/10.1016/j.apenergy.2020.114566>.
- [69] M. Harris, An Investigation on Engine Mass Airflow Sensor Production via TQM, TPM, and Six Sigma Practices, *Oper. Res. Forum* 2 (2021) 61, <https://doi.org/10.1007/s43069-021-00102-y>.